Coenzyme A protects against ferroptosis via CoAlation of mitochondrial thioredoxin reductase

Chao-Chieh Lin[1,2], Yi-Tzu Lin[1,2], Ssu-Yu Chen[1,2], Yasaman Setayeshpour[1,2], Yubin Chen[1,2], Denise E. Dunn[3], Taylor Nguyen[3], Alexander A. Mestre[1,2,4], Adrija Banerjee[5], Lalitha Guruprasad[5], Erik J. Soderblom[6], Guo-Fang Zhang[7,8], Chen-Yong Lin[9], Valeriy Filonenko[10], Suh Young Jeong[11], Scott R. Floyd[3], Susan J. Hayflick[11,12], Ivan Gout[10,13], Jen-Tsan Chi[1, 2] .

[1]Department of Molecular Genetics and Microbiology, [2]Duke Center for Genomic and Computational Biology, [3]Department of Radiation Oncology, [4]Department of Biochemistry, [6]Proteomics and Metabolomics Core Facility, [7]Duke Molecular Physiology Institute and Sarah W. Stedman Nutrition and Metabolism Center, [8]Department of Medicine, Division of Endocrinology, Metabolism, and Nutrition, Duke University School of Medicine, Durham, NC 27710, USA;

[5]School of Chemistry, University of Hyderabad, Hyderabad 500046. India.

[9]Lombardi Comprehensive Cancer Center, Department of Oncology, Georgetown University, 3970 Reservoir Road NW W422 New Research Building, Washington DC 20057, USA.

[10]Department of Cell Signaling, Institute of Molecular Biology and Genetics, National Academy of Sciences of Ukraine, 03680 Kyiv, Ukraine.

[11]Department of Molecular & Medical Genetics, [12]Pediatrics, and Neurology, Oregon Health & Science University, Portland, OR, USA.

[13]Department of Structural and Molecular Biology, University College London, London WC1E 6BT, UK.

Correspondence to: Jen-Tsan Ashley Chi, Department of Molecular Genetics and Microbiology, Center for Genomic and Computational Biology, Duke University School of Medicine, Durham, NC 27710, USA. TEL: +1 (919) 668-4759, e-mail: jentsan.chi@duke.edu

Running title: CoAlation of TXNRD2 regulates ferroptosis

Keywords: CoAlation, ferroptosis, TXNRD2, thioredoxin, mitochondria

Abstract:

The cystine-xCT transporter–glutathione (GSH)–GPX4 axis is the canonical pathway protecting cells from ferroptosis. While GPX4-targeting ferroptosis-inducing compounds (FINs) act independently of mitochondria, xCT-targeting FINs require mitochondrial lipid peroxidation, though the mechanism remains unclear. Since cysteine is also a precursor for coenzyme A (CoA) biosynthesis, here, we demonstrated that CoA supplementation selectively prevented ferroptosis triggered by xCT inhibition by regulating the mitochondrial thioredoxin system. Our data showed that CoA regulated the in vitro enzymatic activity of mitochondrial thioredoxin reductase (TXNRD2) by covalently modifying the thiol group of cysteine (CoAlation) on Cys-483. Replacing Cys-483 with alanine on TXNRD2 abolished its enzymatic activity and ability to protect cells against ferroptosis. Targeting xCT to limit cysteine import and, therefore, CoA biosynthesis reduced CoAlation on TXNRD2. Furthermore, the fibroblasts from patients with disrupted CoA metabolism demonstrated increased mitochondrial lipid peroxidation. In organotypic brain slice cultures, inhibition of CoA biosynthesis led to an oxidized thioredoxin system, increased mitochondrial lipid peroxidation, and loss of cell viability, which were all rescued by ferrostatin-1. These findings identified CoA-mediated post-translational modification to regulate the thioredoxin system as an alternative ferroptosis protection pathway with potential clinical relevance for patients with disrupted CoA metabolism.

Introduction:

The de novo biosynthesis of coenzyme A (CoA) begins with the phosphorylation of extracellular pantothenate (vitamin B5) by pantothenate kinase (PANK), followed by the incorporation of cysteine and ATP(1). Gene mutations in enzymes involved in this pathway—particularly mitochondrial pantothenate kinase 2 *(PANK2*) and CoA synthase (*COASY*)—lead to the neurodegenerative disorders PKAN (Pantothenate Kinase-Associated Neurodegeneration) and CoPAN (COASY Protein-Associated Neurodegeneration), respectively(2). Both PKAN and CoPAN fall under the umbrella of neurodegeneration with brain iron accumulation (NBIA), a group of inherited disorders characterized by progressive dystonia, dysarthria, spasticity, parkinsonism, and other neuropsychiatric symptoms. However, there are currently no effective treatments for PKAN or CoPAN, and their pathogenesis remains poorly understood(3).

CoA and its thioester derivatives are involved in diverse functions, including protein acetylation, the Krebs cycle, amino acid metabolism, fatty acid synthesis, and regulation of gene expression(4). While the cytosolic CoA concentrations are estimated in the micromolar range, mitochondrial CoA levels are substantially higher, up to millimolar concentrations, suggesting a particularly crucial role within mitochondria(5). A recently discovered function of CoA involves its covalent attachment to cysteine residues in proteins under oxidative stress, a post-translational modification termed CoAlation (6). More than 2000 mammalian and bacterial proteins have been identified to be CoAlated(6), yet the regulation and functional consequences of this modification remain largely unclear(7).

In pancreatic tumors, CoA has been proposed to support ferroptosis resistance by enhancing coenzyme Q10 production via the mevalonate pathway(8). Ferroptosis is a regulated form of cell death characterized by iron dependency, oxidative stress, and lipid peroxidation. Most mammalian cells have multiple endogenous ferroptosis-protecting mechanisms. Key among these is the glutathione-dependent antioxidant defense, where glutathione peroxidase 4 (GPX4) reduces lipid hydroperoxides, thus preventing membrane damage and ferroptosis. The xCT antiporter plays a critical role by importing cystine (the dimeric form of cysteine) for GSH synthesis, which is essential for GPX4 function. Additionally, ferroptosis suppression protein 1 (FSP1) provides a GPX4-independent defense by regenerating CoQ10, a lipophilic radical-trapping antioxidant that inhibits lipid peroxidation(9). Therefore, targeting these ferroptosis protection proteins with various ferroptosis-inducing compounds (FINs) may trigger ferroptosis.

FINs can be categorized into different classes based on their targets and mechanisms. Class I FINs (e.g., erastin and sulfasalazine) inhibit the xCT transporter, blocking cystine uptake and depleting glutathione. Class II FINs (e.g., RSL3 and ML162) directly inhibit GPX4. Class III FINs deplete both GPX4 and CoQ10(10). Notably, although both class I and class II FINs impair the xCT-GSH-GPX4 axis, only class I FINs are associated with mitochondrial lipid peroxidation(11, 12). While the requirement of mitochondria for class I FIN-induced ferroptosis has been established, the molecular mechanism remains unclear(11).

The thioredoxin system operates in parallel with the glutathione system to maintain redox balance and suppress ferroptosis (13). The thioredoxin system facilitates the sequential transfer of electrons from NADPH to thioredoxin reductase (TXNRD), then to thioredoxin (TXN), and finally to peroxiredoxins (PRDX), enabling the elimination of intracellular reactive oxygen species (ROS). In mammalian cells, he thioredoxin system is compartmentalized: the cytosolic system consists of TXN1, TXNRD1, and PRDX1, while the mitochondrial system includes TXN2, TXNRD2, and the mitochondrial-specific PRDX3.

Buthionine sulfoximine (BSO) inhibits GSH biosynthesis by targeting γ-glutamylcysteine synthetase but is a much weaker FIN compared to erastin. One study proposed that GSH depletion by BSO leads to cystine accumulation, which enhances the thioredoxin system to counteract ferroptosis(14). This could explain why combining BSO with thioredoxin reductase inhibitors, such as auranofin, leads to synergistic cell death(14). Nevertheless, the precise mechanism underlying this interplay remains to be elucidated.

In this study, we found that CoA effectively prevents class I FIN-induced ferroptosis. CoA availability modulates the redox state of the mitochondrial thioredoxin system, suppressing mitochondrial lipid peroxidation and thereby protecting cells from ferroptosis. Mechanistically, CoA covalently modifies Cys-483 of TXNRD2 via CoAlation, enhancing its enzymatic activity and redox capacity during ferroptotic stress. Consistently, fibroblasts from PKAN patients also exhibited increased mitochondrial lipid peroxidation. These findings were validated in organotypic brain slice cultures (OBSCs), an ex vivo model that preserves cytoarchitecture and neuron-glia interactions. Our work uncovers a class I FIN-specific requirement for mitochondrial lipid peroxidation and identifies cysteine-derived CoA as a critical regulator of thioredoxin redox signaling. These insights may have clinical relevance for PKAN, CoPAN, and other disorders involving CoA metabolism.

Results:

CoA specifically protected against ferroptosis induced by xCT inhibitors

Supplementation of coenzyme A (CoA) in the culture medium has been shown to protect mouse embryonic fibroblasts and pancreatic tumors from ferroptosis(8, 15). Given no known plasma membrane transporter was found, CoA was proposed to be degraded to Pantothenate(16), or 4'-phosphopantetheine (4'-PPT)(17) to increase intracellular CoA. While the detailed mechanism of CoA import remains controversial, we supplemented regular culture media of HT-1080 with two different concentrations of CoA (30 μM and 100 μM) for 18 hours. While previous CoA supplement reports used 200 μM(8) and 500 μM[14] of CoA to rescue ferroptosis, we found that relatively lower doses of CoA supplement (30 μM and 100 μM) were sufficient to increase the intracellular levels of CoA (Figure 1A) and acetyl-CoA (Figure 1B) as measured by mass spectrometry. The increase in acetyl-CoA levels further confirmed that the supplemented CoA could serve as an acetyl group carrier (Figure 1B). Next, we measured the protective capacity of CoA and several canonical ferroptosis inhibitors, including deferoxamine (DFO), ferrostatin-1 (Fer-1), liproxstatin-1 (lipro), and Trolox, against erastin-induced ferroptosis in HT-1080 cells. We found that the ferroptosis protective effect of CoA was comparable to those of the canonical ferroptosis inhibitors (Figure 1C). Subsequently, we further confirmed that CoA also significantly protected against the erastin-induced ferroptosis in six different cancer cell lines (HEK-293, 786-O, H1975, RCC4, MDA-MB-231, and IGROV-1 cells, Supplemental Figure 1, A-F). Consistently, CoA also abolished other molecular features of erastin-induced ferroptosis, including lipid peroxidation (flow cytometry, Figure 1,D and E) and membrane rupture (CellTox Green, Figure 1, F and G). Moreover, we found that CoA inhibited ferroptosis triggered by different class I FINs with distinct chemical structures (erastin, sulfasalazine, and BSO) (Figure 1, C and H, Supplemental Figure 1G) or cystine deprivation (Figure 1, I and J). However, CoA showed only modest or no protective effects against ferroptosis induced by three chemically distinct class II FINs (RSL3, ML162, and JKE-1674) (Figure 1K, Supplemental Figure 1, H and I), class III FIN (FIN56) (Figure 1L), or class IV FIN (FINO2) (Figure 1M). Notably, the effects of CoA on various chemically distinct FINs and cystine deprivation largely excluded the potential off-target effects of CoA on any particular FINs. Interestingly, ionizing radiation and related pathways have been reported to regulate ferroptosis(18-20). We found that CoA also rescued radiation-induced cell death (Supplemental Figure 1J). Taken together, these results indicate that CoA-mediated inhibition of ferroptosis may regulate ferroptosis processes upstream of GPX4, which is targeted by various class II and III FINs.

The mitochondrial thioredoxin system determines CoA-mediated ferroptosis inhibition

To uncover the underlying mechanisms of coenzyme A (CoA)-mediated ferroptosis inhibition, we performed a target compound screen to identify compounds that could abolish CoA-mediated ferroptosis protection. Previously, CoA was proposed to inhibit lipid peroxidation of pancreatic cancer cells by synthesizing coenzyme Q10 for FSP1 via the mevalonate pathway (8). Thus, we first determined whether the CoA-protected ferroptosis could be abolished by FSP1 inhibitor FSEN1 (Supplemental Figure 2A). While FSEN1 was able to sensitize ferroptosis in the control cells, FSEN1 did not abolish CoA-mediated inhibition of ferroptosis in HT-1080 cells (Supplemental Figure 2A). Next, we evaluated the efficacy of various inhibitors targeting pathways recognized to be critical for ferroptosis protection to determine their potential to abolish CoA-mediated ferroptosis protection. These inhibitors included brequinar and teriflunomide(12) (DHO dehydrogenase inhibitors, Supplemental Figure 2, B and C), Etomoxir(21) (β-oxidation inhibitor, Supplemental Figure 2D), methotrexate(22) (dihydrofolate reductase inhibitor, Supplemental Figure 2E), compound C(23) (AMPK inhibitor, Supplemental Figure 2F), TOFA(24) (ACC inhibitor, Supplemental Figure 2G), and the inhibitors of the S-adenosyl homocysteine hydrolase of the trans-sulfuration pathway(25) (Supplemental Figure 2H). However, none of these compounds mitigated the ferroptosis protection effect of CoA (Supplemental Figure 2, A-H). Given that ACSL3 mediates the incorporation of CoA into monounsaturated fatty acids (MUFA)(26, 27), we conducted a genetic knockdown of ACSL3 and found that it had no effect on CoA-mediated protection against ferroptosis (Supplemental Figure 2J).

Among the compounds tested, we found that ferroptocide(28) (thioredoxin inhibitor) abolished CoA-mediated inhibition of ferroptosis (Figure 2A). Furthermore, CoA could not rescue ferroptocide-induced cell death (Supplemental Figure 2K). These data suggest that the thioredoxin system is critical in the CoA-mediated inhibition of ferroptosis. While any screens may have false negatives and our results did not completely rule out the involvement of other pathways, the ability of ferroptocide prompted us to further investigate the thioredoxin pathways. Ferroptocide triggers ferroptosis by inhibiting both the cytosolic and mitochondrial versions of thioredoxin(28). Given thioredoxin and thioredoxin reductase are both required for a functional thioredoxin system, we examined the thioredoxin and thioredoxin reductase activities in HT-1080 cell lysates when treated with erastin, CoA, and their combination (Figure 2B, Supplemental Figure 2L). While thioredoxin activity in HT-1080 cell lysates was not altered by erastin or CoA (Supplemental Figure 2L), erastin significantly reduced thioredoxin reductase (TXNRD) activity which was restored by CoA supplementation (Figure 2B). However, the protein levels of both cytosolic and mitochondrial thioredoxin reductases (TXNRD1 and TXNRD2) were not affected by erastin or CoA (Supplemental Figure 2M). Since erastin was known to reduce the intracellular levels of CoA, we speculated that reduced CoA levels may regulate thioredoxin reductase activity during ferroptosis.

To determine the relative importance of cytosolic versus mitochondrial thioredoxin systems for CoA-mediated inhibition of ferroptosis, we employed pooled siRNA against cytosolic thioredoxin (TXN1) and mitochondrial thioredoxin (TXN2) to knock down these two genes individually (Supplemental Figure 2N). We found that the knockdown of TXN2, but not TXN1, abolished CoA-mediated ferroptosis inhibition (Figure 2C), and this result was further validated using individual TXN2 siRNAs (Supplemental Figure 2O). These data indicate that the mitochondrial thioredoxin system is required for CoA-mediated protection from ferroptosis. To address the concern that siRNA treatment may lead to ferroptosis sensitization in a non-target-dependent manner(29), we conducted CRISPR knockout of TXN2 and found similar abolishment of CoA-mediated ferroptosis inhibition (Supplemental Figure 2P).

While previous findings suggest that unutilized cysteine directly fuels the thioredoxin system to prevent BSO-induced ferroptosis(14), we hypothesized that unutilized cysteine is converted to CoA to regulate ferroptosis. The thioredoxin system transfers electrons in the order of NADPH, TXNRD, TXN, and PRDXs to neutralize intracellular ROS. Given the importance of mitochondrial TXN2 (Figure 2C), we focused on the effects of erastin on the mitochondrial thioredoxin system and examined the protein-protein interaction between TXNRD2 and its substrate TXN2. While TXNRD2 knockout did not alter TXN1 or TXN2 levels (Supplemental Figure 2Q), through co-immunoprecipitation, we found that erastin treatment abolished the interaction between TXNRD2 and TXN2, while CoA supplementation rescued this interaction (Figure 2D). The redox status of the mitochondrial thioredoxin system can be monitored by the monomer (reduced and active)/dimer (oxidized and inactive) ratio of PRDX3(30). Thus, we treated HT-1080 cells with erastin alone or combined with CoA to measure the monomer/dimer ratio of PRDX3 (Figure 2, E and F). We noticed that erastin decreased the monomer (reduced and active form) of mitochondrial PRDX3 (Figure 2, E and F), which was rescued by CoA supplementation (Figure 2, E and F). These results suggest that CoA supplement may inhibit ferroptosis by maintaining the redox function of mitochondrial thioredoxin system.

Simultaneous inhibition of glutathione and CoA synthesis results in synthetic lethality

Our previous findings showed that the knockdown of CoA synthase (COASY) reduced intracellular CoA levels(31). Therefore, we reduced CoA levels by knocking down COASY and assessed the redox status of the mitochondrial thioredoxin system by measuring the monomer/dimer ratio of PRDX3 (Figure 3A). Consistently, COASY knockdown decreased the reduced form (monomer) of PRDX3 (Figure 3B). This reduced monomer/dimer ratio of PRDX3 suggests a defect in mitochondrial thioredoxin function upon erastin treatment (Figure 2, E and F) and COASY knockdown (Figure 3, A and B).

These results prompt us to hypothesize that GSH and CoA may mediate parallel pathways of ferroptosis protection. To determine the contribution of the erastin-depleted GSH and CoA on ferroptosis, we combined BSO (GSH inhibitor) and COASY knockdown (Figure 3C). While BSO itself is known to be a much less potent inducer of ferroptosis, we found that combining BSO with COASY knockdown significantly decreased cell viability over extended incubation, which was rescued by supplementing CoA, or ferrostatin-1 (Figure 3C, Supplemental Figure 3A). 4’-phosphopantetheine (4’-PPT) is an endogenous intermediate metabolite in the CoA biosynthesis pathway which is currently being evaluated as a treatment for PKAN (32). We found that 4’-PPT could also rescue the cell death caused by the BSO and COASY knockdown (Fig 3C). Similarly, a previous report showed that combining BSO (GSH inhibitor) and PANKi(33) (CoA biosynthesis inhibitor) also triggers ferroptosis in pancreatic tumors(8). Therefore, we combined BSO and PANKi and found this combination led to dramatic cell death in HT-1080 cells, which was rescued by CoA, ferroptosis inhibitors (ferrostatin-1, Liproxstatin-1 and Trolox), and mitoTEMPO(34), a mitochondria-targeted antioxidant (Figure 3D, Supplemental Figure 3B). To eliminate the potential off-target effect of BSO, we knocked out the catalytic subunit of GCL (GCLC) and consistently found it also triggered cell death when combined with pharmacological (PANKi, Supplemental Figure 3C) or genetic (siCOASY, Supplemental Figure 3D) inhibition of CoA biosynthesis.

Given that COASY knockdown led to impaired redox status of the mitochondrial thioredoxin system and the relevance of the mitochondrial thioredoxin system for CoA-mediated ferroptosis inhibition (Figure 2C and Figure 3A), we treated HT-1080 cells with PANKi, BSO, or a combination of both. We found that inhibition of CoA synthesis by PANKi, compared with DMSO and BSO, indeed led to robust mitochondrial lipid peroxidation (Figure 3, E and F) and overall lipid peroxidation (Supplemental Figure 3, E and F). Consistently, genetic inhibition of CoA synthesis by COASY siRNA significantly increased mitochondrial lipid peroxidation, which could be abolished by CoA supplementation (Figure 3G). Taken together, while previous findings suggest that cystine/cysteine directly fuels the thioredoxin system to prevent BSO-induced ferroptosis(14), our data indicate that cysteine incorporation in CoA biosynthesis is essential for regulating mitochondrial thioredoxin system to protect against ferroptosis.

CoA supplement increased CoAlation on TXNRD2 and TXNRD2-TXN2 interaction

While the protein levels of thioredoxin reductase remain unchanged, the enzymatic activity of thioredoxin reductase was significantly inhibited by erastin, and such inhibition could be rescued by CoA, suggesting an involvement of post-translational modifications (Figure 2B, Supplemental Figure 2M). Recently, coenzyme A (CoA) has been demonstrated to modify proteins by covalent attachment (CoAlation) to the thiol groups of cysteine residues of various cellular proteins, thereby regulating their enzymatic activities(6). Interestingly, mitochondrial thioredoxin reductase (TXNRD2) is one of the potential CoAlated hits(6). Thus, we raised a monoclonal antibody that specifically recognized CoA and CoAlated proteins (Supplemental Figure 4A). By supplementing CoA in HT-1080 cells overexpressing TXNRD2-V5 and TXN2-myc, we purified TXNRD2 protein by V5 agarose and blotted TXNRD2 protein with CoAlation antibody (Figure 4A). Indeed, TXNRD2 protein showed endogenous level of CoAlation, which was further enhanced by CoA supplementation (Figure 4A). We also found that the thioredoxin 2 (TXN2) protein co-immunoprecipitated with TXNRD2 purification also increased with CoA supplement, suggesting that CoA supplement increases the TXNRD2-TXN2 interaction (Figure 4A). Next, we performed confocal microscopy to assess whether CoA supplementation alters the subcellular localization patterns of endogenous TXNRD2 and TXN2 (Figure 4B). Both TXNRD2 and TXN2 proteins individually localized to mitochondria, as indicated by the COX IV mitochondrial marker. Upon CoA supplementation, we observed increased spatial overlap between TXNRD2 and TXN2 signals within mitochondria, consistent with enhanced interaction (Figure 4B). In contrast to the CoAlation of TXNRD2, other ferroptosis regulators such as FSP1 and GPX4 exhibited no detectable CoAlation (Supplemental Figure 4B).

To verify whether TXNRD2 can be CoAlated in vitro, we purified V5 tagged TXNRD2 protein from HT-1080 cells overexpressing TXNRD2-V5 and incubated with oxidized CoA using a previously published protocol(6). The purified proteins were then separated using native gel and blotted with anti-CoA antibody. We confirmed that TXNRD2 was indeed robustly CoAlated, since treatment with oxidized CoA led to a marked shift in migration behaviors, suggesting structural changes (Supplemental Figure 4C). Next, we ran oxidized CoA-treated TXNRD2 in non-reducing gel and stained with anti-CoA antibody. Consistently, we found that treatment with oxidized CoA dramatically increased TXNRD2 CoAlation. This effect was abolished by dithiothreitol (DTT), which disrupted the disulfide bond of CoAlation (Figure 4C). Next, we examined whether CoAlation of TXNRD2 affects its enzymatic activity (Figure 4D). Indeed, using the in vitro thioredoxin reductase assay, we found that CoAlation on TXNRD2 protein increased enzymatic activity. This effect could be completely inhibited by the thioredoxin reductase inhibitor auranofin(35)(Figure 4D), confirming the specificity. These results suggest that CoA supplement can increase CoAlation on TXNRD2 and TXNRD2-TXN2 interaction.

CoAlation on Cys-483 of TXNRD2 determines its enzymatic activity

To identify the particular CoAlated residue(s) on TXNRD2 protein, we performed a bottom-up mass spectrometry experiment on oxidized CoA-treated tryptic digested TXNRD2 protein (Figure 5, A and B, Supplemental Figure 5A). Compared to untreated control, we identified a dynamic mass modification of +338.07 Da corresponding to fragmented CoA on Cys-483 of TXNRD2 (Figure 5, A and B, Supplemental Figure 5A). Although the searches also included full-length CoA (+762.08 Da), full-length CoA was not identified in these data, possibly due to the instability of the intact structure in the gas phase, causing in-source fragmentation between phosphate groups. The 3D structure of TXNRD2 has been solved(36), and Cys-483 is highly conserved during evolution and does not participate in forming intramolecular disulfide bonds(36). Cys-483 has also been postulated to have a potential redox regulatory role(36). To identify the function of this CoAlation residue, we used site-directed mutagenesis to replace Cys-483 with alanine (C483A) on TXNRD2 and transduced wild-type and the C483A mutant into HT-1080 cells (Figure 5C). Indeed, after protein purification, we found that wild-type TXNRD2 protein had robust endogenous levels of CoAlation signal, which was mostly abolished in C483A mutant (Figure 5C). Similarly, the protein-protein interaction between TXNRD2 and TXN2 was largely decreased by C483A (Supplemental Figure 5B). Also, this endogenous CoAlation signal can be removed by beta-mercaptoethanol (beta-ME) treatment, thereby disassociating CoA from modified Cys-483 and further demonstrating the specificity on this CoAlation signal (Supplemental Figure 5C). Therefore, we tested whether CoAlation on Cys-483 determines the enzymatic activity of TXNRD2 (Figure 5D). Compared with the wild-type TXNRD2 protein, the thioredoxin reductase activity of the C483A CoAlation-null mutant was significantly decreased (Figure 5D). Importantly, this point mutation (C483A) largely abolished the increased thioredoxin reductase activity associated with the treatment of oxidized CoA seen in wild-type TXNRD2 (Fig 5D). Collectively, these data suggest that CoAlation on Cys-483 of TXNRD2 protein determines its thioredoxin reductase activity.

Next, we tested whether CoAlation on TXNRD2 protein could be modulated by cystine/cysteine availability. In TXNRD2-overexpressed HT-1080 cells treated with erastin or cystine deprivation, we found that these treatments indeed decreased CoAlation on purified TXNRD2 (Figure 5E, Supplemental Figure 5D). Similarly, inhibition of CoA biosynthesis by PANKi reduced the CoAlation of TXNRD2 protein (Supplemental Figure 5E).

To demonstrate that CoAlation on TXNRD2 determines cell viability, we performed CRISPR to knock out endogenous TXNRD2 (Supplemental Figure 5F). By treating these cells with erastin or a combination of BSO and PANKi, we found that knockout of TXNRD2 sensitized cells to ferroptosis as determined by cell viability (Figure 5F, Supplemental Figure 5G) or mitochondrial lipid peroxidation (Supplemental Figure 5H). Next, the CRISPR-resistant wild-type or C483A mutant TXNRD2 was re-expressed at similar levels in the TXNRD2-null cells (Supplemental Figure 5F). The erastin or BSO/PANKi sensitizing effects in the TXNRD2-null cells were fully rescued by wild-type TXNRD2 but not C483A mutant in terms of viability (Figure

5F, Supplemental Figure 5G) and mitochondrial lipid peroxidation (Supplemental Figure 5H). These data suggest that CoAlation on the Cys-483 of TXNRD2 protein regulates its enzymatic activity and ferroptosis sensitivity.

To investigate how CoAlation increases TXNRD2 activity, we performed covalent docking on a homology model of human TXNRD2. The best-scoring docking pose showed a covalent bond between the thiol group of Cys483 and the sulfur atom of CoA with a docking score of -4.531 kcal/mol. In addition to Cys483, CoA also interacts with several residues at the dimerization interface, including Glu435, Glu472, Cys500, and Ser501, in the 2D interaction diagram (Supplemental Figure 5I). These interactions suggest that CoA binding could influence the conformational flexibility of the enzyme near its active site.

To assess the stability and dynamic behavior of the TXNRD2–CoA complex, we performed a 250 ns molecular dynamic (MD) simulation. The complex reached equilibrium within the first 50 ns of MD simulations and remained stable throughout the rest of the simulation. Importantly, the covalent bond between CoA and Cys483 was maintained for the entire duration of the simulation, supporting the chemical feasibility of this interaction under physiological conditions. Notably, CoA formed a network of stabilizing non-covalent interactions with the surrounding residues. The primary amine on the adenine of CoA engaged in hydrogen bonding with Gly476. The pantothenate -OH group engaged in hydrogen bonding with Arg492. Also, its adjacent carbonyl oxygen engaged in hydrogen bonding with Gln489. Additionally, the phosphate group at the 3’ position of the ribose ring of CoA established salt bridges with Lys482. Also, the adenine ring makes a π-π stacking interaction with His497 (Supplemental Figure 5J). Together, these interactions contribute to the robust structural integrity of the TXNRD2–CoA complex.

Superimposition of the initial and final structures (Supplemental Figure 5K) revealed a notable conformational change in the C-terminal region, specifically residues Glu412 to Thr518. This region includes key elements involved in catalytic activity and substrate recognition(36). The conformational stabilization observed upon CoA binding suggests a potential mechanistic explanation for the enhanced enzymatic activity. CoA may restrict local flexibility or promote a catalytically favorable alignment of the C-terminal tail, thereby increasing TXNRD2 efficiency.

Disruption of CoA metabolism by PANK inhibition leads to mitochondrial lipid peroxidation and ferroptosis

Mutations in human genes *PANK2* or *COASY*, two genes that encode proteins involved in the CoA biosynthesis pathway, lead to neurodegeneration with brain iron accumulation (NBIA)(2). In particular, mutations in the *PANK2* lead to Pantothenate Kinase-Associated Neurodegeneration (PKAN)(2). The mammalian genome encodes four isozymes that possess pantothenate kinase activity (PANK1α, PANK1β, PANK2, and PANK3). Their tissue expression patterns and subcellular localization have been extensively documented(3). However, the respective cellular roles of each PANK protein and the unique cellular role of *PANK2* mutations in tissue-specific vulnerability leading to PKAN are still unclear. By selectively targeting the glutathione synthesis using BSO, we found that suppressing the mitochondrial thioredoxin system by inhibiting PANK or knocking down COASY significantly increased ferroptosis (Figure 3, C and D) and mitochondrial lipid peroxidation (Figure 3, E-G). To investigate the role of individual PANKs in CoA-directed thioredoxin regulation, we knocked down individual PANK proteins in HT-1080 cells and found that only PANK1 knockdown increased BSO-induced ferroptosis (Figure 6A, Supplemental Figure 6A), without affecting cell proliferation (Supplemental Figure 6B). Surprisingly, by using BSO to selectively target glutathione system, while the fibroblasts from healthy individuals were unaffected, the fibroblasts from PKAN patients showed a substantial decrease in cell viability (Supplemental Figure 6C). Importantly, CoA supplementation was able to rescue the BSO-induced cell death in fibroblasts from PKAN patients (Supplemental Figure 6D). Next, in HT-1080 cells, the knockdown of PANK1 and PANK2, but not PANK3, increased mitochondrial lipid peroxidation to the same level as COASY knockdown (Figure 6B), which was abolished by CoA supplement (Supplemental Figure 6E). Furthermore, we compared mitochondrial ROS and mitochondrial lipid peroxidation in fibroblasts between PKAN patients and healthy individuals (Figure 6, C and D, Supplemental Figure 6, F and G). Surprisingly, we observed increased mitochondrial lipid ROS and mitochondrial lipid peroxidation in fibroblasts from PKAN patients (Figure 6, C and D, Supplemental Figure 6, F and G). While *PANK2* mutation/knockdown may exhibit different responses in cell viability to the stress of BSO-mediated GSH depletion, these data suggest a consistent increase in mitochondrial lipid peroxidation upon *PANK2* mutation/knockdown in PKAN fibroblast and HT-1080 cells.

To bridge the gap between cell-based assays and whole animal models, organotypic brain slice culture (OBSC) has been developed to investigate the mechanisms of diseases and accelerate drug development(37-39). OBSC is an ex vivo model system that preserves the three-dimensional cytoarchitecture and cell-cell interactions of brain tissue. Prepared from neonatal or juvenile rat brains, the slices are typically 100–400 μm thick, which retain a diverse cellular composition, including neurons, astrocytes, microglia, and endothelial cells, enabling the study of complex brain processes in a physiologically relevant context(37-39). OBSC also serves as a model system for studying ferroptosis effects in neurons(40). To mimic the human CoA metabolic defect, we treated rat OBSC with PANKi to inhibit CoA biosynthesis. By monitoring the number and viability of neurons after transfecting OBSC with YFP, we observed that the number of neurons was significantly reduced after PANKi treatment, which could be rescued by the ferroptosis inhibitor, ferrostatin-1 (Figure 6, E and F). These data suggest that inhibition of the thioredoxin system by PANKi itself is sufficient to trigger ferroptosis in the OBSC model. Subsequently, we measured mitochondrial lipid peroxidation and found that mitochondrial lipid peroxidation was consistently increased upon PANKi treatment, which could be abolished through the concurrent application of ferrostatin-1 (Figure 6, G and H). These data suggest that the PANKi triggered mitochondrial lipid peroxidation in neurons in the OBSC model. Finally, we measured the redox status of the mitochondrial form of peroxiredoxin (PRDX3) and found that PANKi downregulated the levels of reduced monomers, which were restored by ferrostain-1 treatment (Figure 6, I and J). While PANKi treatment itself did not induce ferroptosis in the six cancer cell lines (Supplemental Figure 6H), our data suggest that inhibiting CoA biosynthesis may trigger ferroptosis by inducing mitochondrial lipid peroxidation in rat neurons in the OBSC model. Consistently, we found that CoA inhibition also triggered cell death in N27 rat dopaminergic neural cell line (Supplemental Figure 6I), suggesting that neuron cells are more sensitive to CoA inhibition than cancer cells.

Next, we compared the expression of mitochondrial thioredoxin system and important ferroptosis markers in PKAN patients. While PKAN, as a rare genetic disorder, occurs in 1-3 out of 1 million individuals(3), we acquired RNA and protein samples from the fibroblasts of seven PKAN patients in comparison with healthy unaffected individuals. While we did not observe significant differences at RNA levels for *TXNRD2*, *TXN2*, *SLC7A11*, *GCLC*, *GPX4,* and *PTGS2* (Supplemental Figure 6J), we found that TXNRD2 and GPX4 proteins were significantly lower in PKAN patients (Supplemental Figure 6K-L), highlighting a potential clinical relevance of linking CoA synthesis with the mitochondrial thioredoxin system and glutathione system.

Discussion

Since ferroptosis was first described as an iron-dependent, oxidative form of regulated cell death triggered by erastin and other small molecules(41), the role of cystine import, GSH synthesis in suppressing lipid peroxidation through GPX4 has been extensively characterized. Subsequent studies have identified GPX4-independent ferroptosis defense mechanisms, including FSP1-mediated ubiquinone regeneration(9, 42) and the DHODH pathway(12). These studies highlight the existence of parallel, compartmentalized systems that restrict lipid peroxidation in different organelles. Our study adds to this framework by identifying the xCT-cysteine-CoA-TXNRD2 axis as a distinct mitochondrial lipid peroxidation defense mechanism, emphasizing the role of CoA in maintaining mitochondrial redox homeostasis.

CoA was first identified as a ferroptosis inhibitor in p53-mutant cells with increased CoA levels that protect against erastin and glutamate-induced ferroptosis(15). In pancreatic tumor cells, CoA was proposed to protect ferroptosis by enhancing the production of coenzyme Q_{10}, (8). In this study, we found that CoA serves as a protective agent against ferroptosis induced by class I, but not other classes of FINs in multiple cancer cell lines (Figure 1C, Supplemental Figure 1, A-F). Previous studies have found that class I FIN requires mitochondria and their lipid peroxidation to trigger ferroptosis via an unknown mechanism(11, 12). Curiously, while BSO efficiently reduces glutathione synthesis, BSO is a considerably less potent FIN to trigger ferroptosis. One group proposed that GSH inhibition by BSO led to the accumulation of intracellular cysteine levels, which were used by the thioredoxin system to suppress ferroptosis(14). However, the mechanism by which cysteine regulates the thioredoxin system has not been fully elucidated(14). Instead of direct fueling of thioredoxin system by cysteine, our findings suggest that cysteine is incorporated for the biosynthesis of CoA, which protects cells from ferroptosis by CoAlation of TXNRD2 to maintain a mitochondrial thioredoxin function and prevent mitochondrial lipid peroxidation. Thus, xCT-cysteine-CoA-TXNRD2 is an important independent branch of the ferroptosis defense mechanism, distinct from the xCT-GSH-GPX4 axis, that neutralizes mitochondrial lipid peroxidation.

Interestingly, we observed a striking difference in the effects of PANK inhibition between neurons (Figure 6E, Supplemental Figure 6I) and cancer cell lines (Supplemental Figure 6H). While inhibition of either xCT-GSH-GPX4 (by BSO) or xCT-cysteine-CoA-TXNRD2 (by PANKi) alone can be tolerated in cancer cells, their combination leads to synthetic lethality (Figure 3D). Cancer cells were typically isolated and selected for a strong xCT-GSH-GPX4 axis and robust glutathione synthesis that buffers ROS accumulation(43). In contrast, neurons have a weaker xCT-GSH-GPX4 axis due to limited cystine uptake and lower expression of GCL, and rely on astrocytes to maintain glutathione levels(44). Thus, PANKi-induced disruption of CoA biosynthesis in neurons may synergize with their poor glutathione metabolism to drive cell death, while cancer cells remain viable due to their compensatory glutathione systems.

Our data indicate that CoA protects against ferroptosis induced by class I FINs (e.g., erastin, sulfasalazine) but not class II or III FINs, such as GPX4 inhibitors (RSL3, ML162, or FIN56). These findings align with previous studies demonstrating that mitochondria play an essential role in cysteine-deprivation-induced ferroptosis, but are dispensable for ferroptosis induced by GPX4 inhibition[11]. Mechanistically, class I FINs rely on mitochondrial TCA cycle and electron transfer chain activity to drive lipid peroxide generation, while class II FINs bypass mitochondrial function and directly inhibit GPX4, the terminal component of the xCT-GSH-GPX4 axis. Since CoA regulates the mitochondrial thioredoxin system to suppress mitochondrial lipid peroxidation, its effect is limited to the ferroptosis mechanism involving mitochondria.

Protein CoAlation was first identified in 2017 as a reversible post-translational modification in eukaryotic and prokaryotic cells in response to oxidizing environments and metabolic stress(6, 45). So far, CoAlation has been found to inhibit the activity of modified proteins implicated in metabolic or signaling pathways(7). The inhibitory effects of CoAlation have been demonstrated in aconitase, creatine kinase, pyruvate dehydrogenase kinase 2, glyceraldehyde 3-phosphate dehydrogenase, hydroxymethylglutaryl-CoA synthase, Aurora A kinase, and metastasis suppressor protein NME1(6, 7, 46-48). In contrast to these reported inhibitory effects, we found that CoAlation on Cys483 of TXNRD2 increased its thioredoxin reductase activity, which may involve an allosteric mode of activation (Figure 5D). Importantly, CoAlation levels on TXNRD2 respond to the availability of cysteine and CoA as a nutrient-sensing mechanism (Figure 5E, Supplemental Figure 5, D and E). Upon the erastin-induced ferroptosis, CoAlation on TXNRD2 determined cell viability (Figure 5F). Importantly, Cys483 is highly conserved among mammalian TXNRDs(36) and is surface-exposed. Therefore, this residue has been postulated to have a potential redox regulatory role(36). Our findings confirm this prediction that CoAlation on Cys483 is a nutrient-sensing mechanism that adjusts the enzymatic activity of TXNRD2 and ferroptosis sensitivity based on the levels of CoA. Given that Cys483 is highly conserved during evolution (36), redox status regulation by CoAlation may have broader impacts on other TXNRDs across different species, as CoA biosynthesis is an ancient pathway conserved across different domains of life(49).

These mechanistic insights into CoA-CoAlation-TXNRD2 signaling offer a promising direction for therapeutic intervention. Small molecules that modulate CoA synthesis or mimic CoAlation on TXNRD2 could potentially be developed as ferroptosis inhibitors specifically targeting the redox status of mitochondria, especially for neurodegenerative diseases where ferroptosis plays a pathogenic role(50). Conversely, disrupting this pathway may sensitize cancer cells to ferroptosis-inducing agents, offering a synthetic lethality approach when combined with xCT inhibitors (9, 51). Furthermore, because CoAlation responds to cellular metabolic state(6), it may serve as a pharmacodynamic marker to stratify patients or monitor treatment efficacy in ferroptosis-targeted therapies, much like redox-sensitive PTMs that are increasingly used to evaluate drug response in metabolic and oxidative stress conditions(52).

NBIA is a group of rare neurodegenerative disorders with increased basal ganglia iron on brain magnetic resonance imaging(53). NBIA is associated with mutations in different enzymes involved in the CoA biosynthesis, including *PANK2* and *COASY*. Mutations in *PANK2*, a key mitochondrial enzyme involved in CoA biosynthesis, account for approximately half of NBIA cases(53). Given that iron is essential for ferroptosis via the Fenton reaction, it is reasonable to speculate on a relationship between ferroptosis and PKAN/NBIA. Consistently, PKAN astrocytes were found to be prone to ferroptosis with higher oxidized proteins and malondialdehyde(54). However, a direct connection between disrupted CoA metabolism and ferroptosis during PKAN is still lacking. In this study, we found that *PANK2* knockdown increased mitochondrial lipid peroxidation in HT-1080 cells (Figure 6B). Even though PKAN patients showed no reduction in CoA levels in fibroblasts(3), we still observed increased mitochondrial lipid peroxidation (Figure 6, C and D) that may predispose these cells to ferroptosis. Indeed, fibroblasts from PKAN patients are more sensitive to BSO-mediated glutathione depletion (Supplemental Fig 6C). We also found that OBSC treated with PANKi exhibited many features associated with PKAN/NBIA, including a reduced number of neurons, increased mitochondrial lipid peroxidation, and disrupted thioredoxin systems (Figure 6, E-J). Importantly, the application of ferrostatin-1 to rescue these phenotypes implies that PANKi-induced cell death is caused by ferroptosis (Figure 6, E-J). These data also suggest that we have developed an OBSC model targeting all PANKs to complement current models of PKAN and NBIA. With the development of PANK2-specific inhibitors in the future or genetic removal of *PANK2*, this OBSC model can be further developed to reveal the mechanistic underpinnings and therapeutic agents. These findings not only support ferroptosis as a potential pathogenic mechanism in NBIA/PKAN, but also open the door to testing various ferroptosis inhibitors, like ferrostatin-1, as candidate neuroprotective agents in these disorders. Moreover, the pharmacologic strategies to modulate CoAlation, such as developing novel pantothenate kinase inhibitors or small-molecule CoA analogs, could offer an innovative means to overcome ferroptosis resistance in a disease or tissue specific manner. Together, inhibiting ferroptosis and targeting CoAlation pathways may have significant therapeutic implications.

Methods

Sex as a biological variable

Our study examined the brain slices of both male and female rats, and similar findings are reported for both sexes.

Mass spectrometry

CoA and acetyl-CoA were extracted from 30 million cells per sample using previously published methods(55). The cell pellets were treated with 300 µL of ice-cold 0.1M KH2PO4. Methanol containing 10% acetic acid was added to the cell pellets, followed by solid phase extraction (SPE). For the SPE process, 1 ml ion exchange cartridge packed with 100 mg of 2–2(pyridyl)ethyl silica gel (Sigma) was activated with 1 ml of methanol and equilibrated with 1 ml of buffer A (methanol/H_2O 1:1, containing 5% acetic acid). The sample extract was loaded onto the cartridge, and additional steps with buffer A, buffer B (methanol/H_2O 1:1, 50 mM ammonium formate), buffer C (methanol/H_2O 3:1, 50 mM ammonium formate), and methanol were performed. The eluent (3 ml) was collected and dried using N_2 gas. The resulting dried residue was re-suspended in 100 µl of H_2O for LC-MS/MS analysis(55, 56).

For CoAlation site identification on TXNRD2, HT-1080 cells overexpressing TXNRD2-v5 were lysed with NP-40 buffer containing 25 mM N-ethylmaleimide (NEM, 23030, Thermo Fisher) and protease inhibitor (04693116001, Roche) at 4 degree with constant shaking. The lysates were then centrifuged at 21,000 g for 10min, and the supernatant was purified by V5-tagged Protein Purification Kit (3317, MBL) and eluted by v5 peptide. Purified TXNRD2 was incubated with 10 mM oxidized CoA in 50 mM Tris-HCl (pH 7.5) at room temperature for 30 min. The samples with/without oxidized CoA treatment were then resolved on a 12% non-reducing SDS

PAGE. After colloidal blue staining (LC6025, Thermo fisher), the bands with ~50kD were cut for Mass spectrometry.

The bands obtained from SDS-PAGE gels underwent in-gel tryptic digestion following established protocols. Post-digestion, peptides were dehydrated and then reconstituted in a solution containing 0.2% formic acid and 2% acetonitrile at a volume of 12 uL. Each resulting sample underwent chromatographic separation using a Waters MClass UPLC, utilizing a 1.7 µm HSS T3 C18 75 µm I.D. X 250 mm reversed-phase column (NanoFlow data). The mobile phase for chromatography consisted of two components: (A) 0.1% formic acid in water and (B) 0.1% formic acid in acetonitrile. Injection of 3 µL of the sample commenced the process, with peptides initially captured for 3 minutes on a 5 µm Symmetry C18 180 µm I.D. X 20 mm column at a rate of 5 µl/min, with a composition of 99.9% A. Following this, an analytical column was engaged, and a linear elution gradient ranging from 5% B to 40% B occurred over 60 minutes at a flow rate of 400 nL/min.

The Fusion Lumos mass spectrometer (Thermo) was connected to the analytical column via an electrospray interface, functioning in a data-dependent acquisition mode. The instrument settings included a precursor MS scan from m/z 375-1500 at R=120,000 (target AGC 2e5, max IT 50 ms), with subsequent MS/MS spectra acquired in the ion trap (target AGC 1e4, max IT 100 ms). HCD energy settings were consistently maintained at 30v for all experiments, and a dynamic exclusion of 20 seconds was implemented to avoid re-analysis of previously fragmented precursor ions.

The LC-MS/MS data files obtained were processed using Proteome Discoverer 3.0 (Thermo Scientific) and subsequently subjected to independent Sequest database searches against a comprehensive Human protein database. This database included both forward (20260 entries) and reverse entries for each protein. The search parameters allowed for 2 ppm tolerance for precursor ions and 0.8 Da tolerance for product ions, employing trypsin specificity with allowance for up to two missed cleavages. Dynamic mass modifications were defined for Cleaved CoA (+338.07 Da on C) and full-length CoA (+762.08 Da on C). All spectra derived from the searches were imported into Scaffold (v5.3, Proteome Software), where scoring thresholds were adjusted to maintain a peptide false discovery rate of 1%, utilizing the PeptideProphet algorithm. Additionally, the raw data was imported into Skyline (MacCoss Lab, UWash) for the purpose of measuring extracted ion chromatograms of modified peptides.

Chemicals

Auranofin (A6733, Sigma); ferroptocide (F1293, TCI); PANKi (31002, Cayman); CoA (F15115, Astatech); erastin (5499, Bio-techne); BSO (B2515, Sigma); RSL3 (19288, Cayman); ML162 (20455, Cayman); FIN56 (25180, Cayman); ferrostatin-1 (17729, Cayman); liproxstatin-1 (17730, Cayman); Trolox (218940010, Thermo Fisher); lovastatin (S2061, Selleckchem); simvastatin (S1792, Selleckchem); iFSP1 (29483, Cayman); brequinar (S3565, Selleckchem); Teriflunomide (S4169, Selleckchem); Methotrexate (S1210, Selleckchem); Compound C (S7306, Selleckchem); TOFA (S6690, Selleckchem); Etomoxir sodium salt (S8244, Selleckchem); 3-Deazaadenosine (HY-W013332A, Medchemexpress); 3-Deazaneplanocin A (HY-12186, Medchemexpress); Adenosine dialdehyde (HY-123055, Medchemexpress).

In vitro assay

To determine thioredoxin activity in cell lysate, after the treatment of erastin, CoA, or in combination, 30 million cells per sample were washed with PBS and homogenized in 500µl of cold buffer (100 mM Tris-HCl, pH7.5, 1 mM EDTA) with protease inhibitor. After 15 minutes of centrifugation (10,000g, 4 degree Celsius), the thioredoxin activity in the supernatant was determined by Thioredoxin Fluorometric Activity Assay Kit (500228, Cayman). To determine thioredoxin reductase activity in cell lysate, after the treatment of erastin, CoA, or in combination, 30 million cells per sample were washed with PBS and homogenized in 500µl of cold buffer (50 mM potassium phosphate, pH 7.4, 1 mM EDTA) with protease inhibitor. After 15 minutes of centrifugation (10,000g, 4 degree Celsius), the thioredoxin activity in the supernatant was determined by Thioredoxin Reductase Colorimetric Assay Kit (10007892, Cayman). To determine thioredoxin reductase activity in purified TXNRD2 protein, HT-1080 cells transduced with TXNRD2 Wild-type or C483A mutant were lysed with NP-40 buffer with protease inhibitor and 25 mM NEM. After centrifugation, the supernatant was purified by V5-tagged Purification Kit Ver.2 (3317, MBL). The purified TXNRD2 protein was resolved by non-reducing SDS PAGE to confirm equal amount of input for Thioredoxin Reductase Colorimetric Assay Kit (10007892, Cayman).

Cell culture

HT-1080, HEK-293, 786-O, H1975, RCC4, and MDA-MB-231 cells were obtained from Duke University's Cell Culture Facility and authenticated by STR profiling. Prior to freezing, these cell lines were authenticated using STR DNA profiling to ensure their identity and confirmed to be free from mycoplasma contamination by the Cell Culture Facility. The cells were cultured for a duration of less than 6 months. Human fibroblasts from healthy individuals were obtained from Coriell Institute for Medical Research. The fibroblasts from PKAN patients were provided by Dr. Susan J. Hayflick. All fibroblast collection is part of Duke's IRB-approved protocol Pro00101047. All cell lines were maintained in a humidified incubator at 37°C with 5% CO2 in DMEM (GIBCO-11995) supplemented with 10% heat-inactivated fetal bovine serum (#10082147, ThermoFisher) and antibiotics (streptomycin, 10,000 UI/ml and penicillin, 10,000 UI/ml, #15140122, ThermoFisher).

Constructs and lentivirus viral infections

Small interfering RNAs (siRNAs) targeting human *COASY*, *TXN1*, *TXN2*, *ACSL3*, and *ACSL4* RNA were obtained from Dharmacon (D-006751-01, D-006751-02, M-006340-01-0005, M-017448-00-0005, M-010061-00-0005, M-009364-00-0005). The guide RNA targeting TXNRD2, TXN2, and GCLC was purchased from Sigma (HSPD0000063630, HSPD0000075931, and HSPD0000016313 in GeCKOv2 all-in-one lentiviral plasmid). The TXNRD2 cDNA in PLX304 was procured from DNASU (HsCD00446697). To generate guide RNA-resistant TXNRD2 (with synonymous mutation) and point mutant (TXNRD2 C483A), we employed the QuikChange II XL Site-Directed Mutagenesis Kit (#200521, Agilent). Lentivirus expressing specific constructs was produced by transfecting HEK-293 cells in 6-well plates with a 1:1:0.1 ratio of lentiviral vector:pMD2.G:psPAX2 using the TransIT-LT1 transfection reagent (Mirus). Subsequently, the lentivirus was filtered through a cellulose acetate membrane (0.45 µm, #28145-481, VWR), and 250 µl of media containing the lentivirus were added to a 60mm dish of the indicated cells along with polybrene (8 µg/ml) and selected with puromycin or blasticidin.

Cell viability and cytotoxicity

Cell viability was assessed using the CellTiter-Glo luminescent cell viability assay (Promega) according to the manufacturer's instructions. Briefly, 15 µl of CellTiter-Glo substrate was added to cells cultured in a 96-well plate with 100 µl of media, followed by 10 minutes of shaking. The signal intensity was measured using a chemiluminescence plate reader. For quantification of cell death, the CellTox Green assay (Promega) was performed. The dye was added to the media at a 1:1000 dilution, and cell death was quantified using a fluorescence plate reader. To determine the level of GSH (glutathione), the GSH/GSSG-Glo Assay (Promega) was conducted according to the manufacturer's guidelines. Briefly, the samples in a 96-well plate were treated with a lysis reagent specific to each measurement set: total glutathione lysis reagent for total glutathione measurement and oxidized glutathione lysis reagent for GSSG measurement. Afterward, Luciferin Generation Reagent was added to all wells, and the assays were mixed and incubated for 30 minutes. Following this, Luciferin Detection Reagent was added to all wells, and luminescence was measured after a 15-minute incubation. GSH/GSSG ratios were directly calculated from the luminescence measurements (in relative light units, RLU).

Western blots

Protein concentrations were quantified by BCA assay (#23227, ThermoFisher). After protein extraction, the samples were loaded on 12% native, non-reducing, or reducing SDS-PAGE gels, transferred to PDVF membrane, blocked with 5% non-fat milk in 1xTBST, incubated with primary antibodies overnight at 4°C. Primary antibodies: COASY (1:1000, sc-393812, Santa Cruz); PRDX1 (1:1000, 15816-1-AP, Proteintech); PRDX3 (1:1000, 10664-1-AP, Thermo Fisher); GAPDH (1:2000, sc-25778, Santa Cruz); TXNRD1 (1:1000, 11117-1-AP, Santa Cruz); TXNRD2 (1:1000, PA529458, Thermo Fisher); v5 (1:1000, MA5-15253, ThermoFisher); alpha Tubulin (1:1000, sc-32293, Santa Cruz). We generated the CoAlation antibody used in this study, which is commercially available from ProtTech (Clone 567A19-12G9, PT-mAb-CoA, ProtTech). TXNRD2 protein was purified from HT-1080 cells overexpressing TXNRD2-v5 by V5-tagged Protein Purification Kit Ver.2 (3317, MBL). For TXNRD2 purification, HT-1080 cells were lysed by NP-40 buffer with 25 mM N-ethylmaleimide (NEM, 23030, Thermo Fisher) and protease inhibitor (04693116001, Roche) in 4 degree with constant shaking. The lysates were then centrifuged at 21,000 g for 10min, and the supernatant was purified by V5-tagged Protein Purification Kit. For PRDX blots, the cells were washed with PBS and incubated in NEM buffer (HEPES, pH 7.4 40mM, NaCl 50 mM, EDTA 1mM, EGTA 1mM, NEM 100 mM, protease inhibitor) for 10 min. CHAPS (1%) was then added to lyse the cells for quantification.

Confocal microscopy

IGROV-1 cells ± CoA supplement were washed twice with PBS and fixed in 3.7 % paraformaldehyde for 20 min. The samples were permeabilized and blocked with 0.2% Triton X-100 and 2% BSA for 30 min. Primary antibodies were incubated with the cells for 1 hour. Confocal microscopy was performed using LSM 880 with airyscan (Zeiss). Antibody: TXNRD2 (1:100, PA529458, Thermo Fisher); TXN2 (1:100, sc-133201, Santa Cruz); COX IV with direct AF594 Conjugate (1:100, 8692S, Cell Signaling).

Quantitative real-time PCR

The RNA extraction and purification were carried out using the RNeasy Mini Kit (Qiagen) following the manufacturer's recommended protocol. Subsequently, reverse transcription to cDNA was performed using random hexamers and SuperScript IV reverse transcriptase (Invitrogen). For quantitative real-time PCR analysis, the cDNA was combined with primers and Power SYBR Green PCR Mix (Applied Biosystems), and the reactions were run on a StepOnePlus Real-time PCR system (Applied Biosystems). Each sample was technically triplicated to obtain the mean +/- standard error of the mean (SEM). The data presented are representative of a minimum of two independent experimental repetitions. Primer sequences are listed in Supplemental Table 1.

Lipid peroxidation assay

Lipid peroxidation was assessed using C11-BODIPY staining following the manufacturer's instructions (D3861, ThermoFisher Scientific). Briefly, cells were exposed to either a vehicle control or treatments for 16 hours. Subsequently, the medium was replaced with a 10μM C11-BODIPY-containing medium and incubated for 1 hour. After harvesting, washing, and resuspension in PBS containing 1% BSA, the levels of lipid peroxidation were quantified using flow cytometry (FACSCanto TM II, BD Biosciences). Similarly, for mitochondrial lipid peroxidation, mitoPerOx(57) (200 nM,18798, Cayman) containing medium was incubated with cells for 30 min.

Protein Structure Preparation

The sequence of *Homo sapiens* mitochondrial thioredoxin reductase 2 (TXNRD2) was obtained from the NCBI database with NCBI ID: NP_006431.2. The Swiss-Model web server was used to model the dimeric structure based on the crystal structure of *Mus musculus* TXNRD (PDB_ID: 3DGZ) as the template. In the monomeric model protein, the bond orders were adjusted, hydrogen atoms were added, charges were assigned and OPLS4 force field was used for optimization and energy minimization using Schrödinger Maestro.

Molecular Docking

The LigPrep module in Schrödinger Maestro was used to generate the coenzyme A (CoA) structure. The 2D coordinates were converted to 3D, the force field geometry was optimized using the OPLS4 force field and hydrogen atoms were added. Molecular docking of CoA on the monomeric TXNRD2 was performed using the Covalent docking module. The number of CoA docking poses was set to 10.

Molecular dynamics simulations

Molecular dynamics (MD) simulations were performed for the TXNRD2-CoA complex using the Desmond module of Schrödinger Maestro for 250 ns at 300 K temperature and 1.01325 bar pressure. The complex was solvated in an orthorhombic box measuring 10Å ×10Å × 10Å with the TIP3P water model, and the system was neutralized by adding Na^+ ions.

Organotypic brain slice cultures

The experiment involved the use of CD Sprague-Dawley rat pups at postnatal day 10, obtained from Charles River (Wilmington, MA). The rat brains were sliced into 250 µm coronal sections using Vibratomes from Vibratome Co. (St. Louis, MO) in chilled medium baths. Each rat brain yielded approximately 6 slices, which were further divided into "hemi-coronal" slices. These slices were individually placed in multi-well plates, resulting in 12 brain slice assays per rat brain.

To establish the brain slice assays, the slices were explanted in an interface configuration using culture medium containing 15% heat-inactivated horse serum, 10 mM KCl, 10 mM HEPES, 100 U/ml penicillin/streptomycin, 1 mM MEM sodium pyruvate, and 1 mM L-glutamine in Neurobasal A (Invitrogen, Carlsbad, CA). Before use, the medium was filter sterilized at 0.22 µm.

The 12-well plates used for plating the slices provided culture support through a low concentration of agarose (0.5%; J.T. Baker, Phillipsburg, NJ). The slice cultures were maintained in humidified incubators at 32 °C under 5% CO2.

To label healthy neurons, YFP was transfected using a biolistic device (Bio-Rad Helios Gene Gun). Following the treatment of PANKi or a combination of PANKi with ferrostatin-1, neurons expressing YFP were observed and visualized under fluorescence microscopy after 1 day of incubation. Neuronal viability was assessed by fluorescence microscopy: the number of YFP-positive neurons remaining after treatment was quantified as a measure of cell survival. All work performed on Sprague-Dawley pup for OBSC was approved by the Institutional Animal Care and Use Committee at Duke University.

Statistical analysis

The bar graphs display individual data points, each representing the number of biological replicates as indicated. The line graph includes the number of biological replicates specified in the figure legends. All data are presented as the mean +/- the standard error of the mean (SEM). Statistical significance was determined using Graphpad software with one-way ANOVA and Tukey's multiple comparisons, two-way ANOVA with Sidak's multiple comparisons, or a two-tailed Student's t-test, as appropriate. The error bars on the graphs represent the SEM, and significance between samples is denoted as $*p < 0.05$, $**p < 0.01$, $***p < 0.001$, and $****p < 0.0001$.

Study approval

All animal procedures, including the preparation of organotypic brain-slice cultures from Sprague-Dawley rat pups, were reviewed and approved by the Duke University Institutional Animal Care and Use Committee (IACUC), Durham, NC, USA, under protocol number A233–23-11. Rats were housed in Duke’s AAALAC-accredited animal care facility and received daily care under the supervision of veterinary staff from the Division of Laboratory Animal Resources. All animal experiments complied with the U.S. Animal Welfare Act, the Public Health Service Policy on Humane Care and Use of Laboratory Animals, and the NIH Guide for the Care and Use of Laboratory Animals (8th edition).

Human primary dermal fibroblast lines from patients and healthy controls were obtained with written informed consent and collected under OHSU’s IRB-approved repository protocol

#7232 (Oregon Health & Science University, Portland, OR, USA). These de-identified samples were shared with Duke University under appropriate material transfer agreements. Additional de-identified human fibroblast lines were obtained under an exempt protocol approved by the Duke University Health System Institutional Review Board (DUHS IRB), Durham, NC, USA (protocol Pro00101047), and are not considered human-subjects research.

Data availability

The authors are prepared to provide all data and reagents supporting the study's findings upon a reasonable request. Mass spectrometry data are deposited in the ProteomeXchange Consortium under ID PXD062566. Supporting data values are available in the supplementary document.

Author contributions

C.C.L. and J.T.C. conceived the experiments and wrote the manuscript. C.C.L. performed the majority of the experiments. J.T.C. supervised the work. Y.T.L., S.Y.C., Y.S., Y.C., D.E.D., T.N., A.A.M., A.B., L.G., E.J.S., S.F., S.Y.J., V.F., and G.Z. collaborated in the discussion and experiments. C.Y.L. provided critical reagents. S.J.H. and I.G. provided critical feedback.

Acknowledgments

We are grateful for technical support from the members of the Chi lab and Zih-Syuan Wu from National Defense Medical Center. We acknowledge the financial support in part by DCI Pilot Project, DOD grants (W81XWH-17-1-0143, W81XWH-15-1-0486, W81XWH-19-1-0842, W81XWH-20-1-0907) and NIH grants (R01GM124062, 1R01NS111588-01A1, 1R21-AI149205).

Conflict of interest statement

The authors have declared that no conflict of interest exists.

References

1. Leonardi R, and Jackowski S. Biosynthesis of Pantothenic Acid and Coenzyme A. *EcoSal Plus.* 2007;2(2).
2. Hayflick SJ. Pantothenate kinase-associated neurodegeneration (formerly Hallervorden-Spatz syndrome). *J Neurol Sci.* 2003;207(1-2):106-7.
3. Hayflick SJ, Jeong SY, and Sibon OCM. PKAN pathogenesis and treatment. *Mol Genet Metab.* 2022;137(3):283-91.
4. Gout I. Coenzyme A, protein CoAlation and redox regulation in mammalian cells. *Biochem Soc Trans.* 2018;46(3):721-8.
5. Leonardi R, Zhang YM, Rock CO, and Jackowski S. Coenzyme A: back in action. *Prog Lipid Res.* 2005;44(2-3):125-53.
6. Tsuchiya Y, Peak-Chew SY, Newell C, Miller-Aidoo S, Mangal S, Zhyvoloup A, Bakovic J, Malanchuk O, Pereira GC, Kotiadis V, et al. Protein CoAlation: a redox-regulated protein modification by coenzyme A in mammalian cells. *Biochem J.* 2017;474(14):2489-508.
7. Filonenko V, and Gout I. Discovery and functional characterisation of protein CoAlation and the antioxidant function of coenzyme A. *BBA Adv.* 2023;3(100075.
8. Badgley MA, Kremer DM, Maurer HC, DelGiorno KE, Lee HJ, Purohit V, Sagalovskiy IR, Ma A, Kapilian J, Firl CEM, et al. Cysteine depletion induces pancreatic tumor ferroptosis in mice. *Science.* 2020;368(6486):85-9.
9. Bersuker K, Hendricks JM, Li Z, Magtanong L, Ford B, Tang PH, Roberts MA, Tong B, Maimone TJ, Zoncu R, et al. The CoQ oxidoreductase FSP1 acts parallel to GPX4 to inhibit ferroptosis. *Nature.* 2019;575(7784):688-92.
10. Gan B. Mitochondrial regulation of ferroptosis. *J Cell Biol.* 2021;220(9).
11. Gao M, Yi J, Zhu J, Minikes AM, Monian P, Thompson CB, and Jiang X. Role of Mitochondria in Ferroptosis. *Mol Cell.* 2019;73(2):354-63 e3.
12. Mao C, Liu X, Zhang Y, Lei G, Yan Y, Lee H, Koppula P, Wu S, Zhuang L, Fang B, et al. DHODH-mediated ferroptosis defence is a targetable vulnerability in cancer. *Nature.* 2021;593(7860):586-90.
13. Lu J, and Holmgren A. The thioredoxin antioxidant system. *Free Radic Biol Med.* 2014;66(75-87.
14. Harris IS, Treloar AE, Inoue S, Sasaki M, Gorrini C, Lee KC, Yung KY, Brenner D, Knobbe-Thomsen CB, Cox MA, et al. Glutathione and thioredoxin antioxidant pathways synergize to drive cancer initiation and progression. *Cancer Cell.* 2015;27(2):211-22.
15. Leu JI, Murphy ME, and George DL. Mechanistic basis for impaired ferroptosis in cells expressing the African-centric S47 variant of p53. *Proc Natl Acad Sci U S A.* 2019;116(17):8390-6.
16. Naquet P, Kerr EW, Vickers SD, and Leonardi R. Regulation of coenzyme A levels by degradation: the 'Ins and Outs'. *Prog Lipid Res.* 2020;78(101028.
17. Srinivasan B, Baratashvili M, van der Zwaag M, Kanon B, Colombelli C, Lambrechts RA, Schaap O, Nollen EA, Podgorsek A, Kosec G, et al. Extracellular 4'-phosphopantetheine is a source for intracellular coenzyme A synthesis. *Nat Chem Biol.* 2015;11(10):784-92.
18. Ye LF, Chaudhary KR, Zandkarimi F, Harken AD, Kinslow CJ, Upadhyayula PS, Dovas A, Higgins DM, Tan H, Zhang Y, et al. Radiation-Induced Lipid Peroxidation Triggers Ferroptosis and Synergizes with Ferroptosis Inducers. *ACS Chem Biol.* 2020;15(2):469-84.
19. Chen PH, Tseng WH, and Chi JT. The Intersection of DNA Damage Response and Ferroptosis-A Rationale for Combination Therapeutics. *Biology (Basel).* 2020;9(8).

20. Chen PH, Wu J, Ding CC, Lin CC, Pan S, Bossa N, Xu Y, Yang WH, Mathey-Prevot B, and Chi JT. Kinome screen of ferroptosis reveals a novel role of ATM in regulating iron metabolism. *Cell Death Differ.* 2019;27(27):1008-22.
21. Kagan VE, Mao G, Qu F, Angeli JP, Doll S, Croix CS, Dar HH, Liu B, Tyurin VA, Ritov VB, et al. Oxidized arachidonic and adrenic PEs navigate cells to ferroptosis. *Nat Chem Biol.* 2017;13(1):81-90.
22. Soula M, Weber RA, Zilka O, Alwaseem H, La K, Yen F, Molina H, Garcia-Bermudez J, Pratt DA, and Birsoy K. Metabolic determinants of cancer cell sensitivity to canonical ferroptosis inducers. *Nat Chem Biol.* 2020;16(12):1351-60.
23. Lee H, Zandkarimi F, Zhang Y, Meena JK, Kim J, Zhuang L, Tyagi S, Ma L, Westbrook TF, Steinberg GR, et al. Energy-stress-mediated AMPK activation inhibits ferroptosis. *Nat Cell Biol.* 2020;22(2):225-34.
24. Liang D, Feng Y, Zandkarimi F, Wang H, Zhang Z, Kim J, Cai Y, Gu W, Stockwell BR, and Jiang X. Ferroptosis surveillance independent of GPX4 and differentially regulated by sex hormones. *Cell.* 2023;186(13):2748-64 e22.
25. Cao J, Chen X, Jiang L, Lu B, Yuan M, Zhu D, Zhu H, He Q, Yang B, and Ying M. DJ-1 suppresses ferroptosis through preserving the activity of S-adenosyl homocysteine hydrolase. *Nat Commun.* 2020;11(1):1251.
26. Doll S, Proneth B, Tyurina YY, Panzilius E, Kobayashi S, Ingold I, Irmler M, Beckers J, Aichler M, Walch A, et al. ACSL4 dictates ferroptosis sensitivity by shaping cellular lipid composition. *Nat Chem Biol.* 2017;13(1):91-8.
27. Magtanong L, Ko PJ, To M, Cao JY, Forcina GC, Tarangelo A, Ward CC, Cho K, Patti GJ, Nomura DK, et al. Exogenous Monounsaturated Fatty Acids Promote a Ferroptosis-Resistant Cell State. *Cell Chem Biol.* 2019;26(3):420-32 e9.
28. Llabani E, Hicklin RW, Lee HY, Motika SE, Crawford LA, Weerapana E, and Hergenrother PJ. Diverse compounds from pleuromutilin lead to a thioredoxin inhibitor and inducer of ferroptosis. *Nat Chem.* 2019;11(6):521-32.
29. von Massenhausen A, Schlecht MN, Beer K, Maremonti F, Tonnus W, Belavgeni A, Gavali S, Flade K, Riley JS, Zamora Gonzalez N, et al. Treatment with siRNAs is commonly associated with GPX4 up-regulation and target knockdown-independent sensitization to ferroptosis. *Sci Adv.* 2024;10(11):eadk7329.
30. Kameritsch P, Singer M, Nuernbergk C, Rios N, Reyes AM, Schmidt K, Kirsch J, Schneider H, Muller S, Pogoda K, et al. The mitochondrial thioredoxin reductase system (TrxR2) in vascular endothelium controls peroxynitrite levels and tissue integrity. *Proc Natl Acad Sci U S A.* 2021;118(7).
31. Lin CC, Kitagawa M, Tang X, Hou MH, Wu J, Qu DC, Srinivas V, Liu X, Thompson JW, Mathey-Prevot B, et al. CoA synthase regulates mitotic fidelity via CBP-mediated acetylation. *Nat Commun.* 2018;9(1):1039.
32. Jeong SY, Hogarth P, Placzek A, Gregory AM, Fox R, Zhen D, Hamada J, van der Zwaag M, Lambrechts R, Jin H, et al. 4'-Phosphopantetheine corrects CoA, iron, and dopamine metabolic defects in mammalian models of PKAN. *EMBO Mol Med.* 2019;11(12):e10489.
33. Sharma LK, Leonardi R, Lin W, Boyd VA, Goktug A, Shelat AA, Chen T, Jackowski S, and Rock CO. A high-throughput screen reveals new small-molecule activators and inhibitors of pantothenate kinases. *J Med Chem.* 2015;58(3):1563-8.
34. Liu X, Subedi KP, Zheng C, and Ambudkar I. Mitochondria-targeted antioxidant protects against irradiation-induced salivary gland hypofunction. *Sci Rep.* 2021;11(1):7690.

35. Gandin V, Fernandes AP, Rigobello MP, Dani B, Sorrentino F, Tisato F, Bjornstedt M, Bindoli A, Sturaro A, Rella R, et al. Cancer cell death induced by phosphine gold(I) compounds targeting thioredoxin reductase. *Biochem Pharmacol.* 2010;79(2):90-101.
36. Biterova EI, Turanov AA, Gladyshev VN, and Barycki JJ. Crystal structures of oxidized and reduced mitochondrial thioredoxin reductase provide molecular details of the reaction mechanism. *Proc Natl Acad Sci U S A.* 2005;102(42):15018-23.
37. Varma H, Lo DC, and Stockwell BR. High throughput screening for neurodegeneration and complex disease phenotypes. *Comb Chem High Throughput Screen.* 2008;11(3):238-48.
38. Daviaud N, Garbayo E, Schiller PC, Perez-Pinzon M, and Montero-Menei CN. Organotypic cultures as tools for optimizing central nervous system cell therapies. *Exp Neurol.* 2013;248(429-40.
39. Croft CL, Futch HS, Moore BD, and Golde TE. Organotypic brain slice cultures to model neurodegenerative proteinopathies. *Mol Neurodegener.* 2019;14(1):45.
40. Venkatesh D, O'Brien NA, Zandkarimi F, Tong DR, Stokes ME, Dunn DE, Kengmana ES, Aron AT, Klein AM, Csuka JM, et al. MDM2 and MDMX promote ferroptosis by PPARalpha-mediated lipid remodeling. *Genes Dev.* 2020;34(7-8):526-43.
41. Dixon SJ, Lemberg KM, Lamprecht MR, Skouta R, Zaitsev EM, Gleason CE, Patel DN, Bauer AJ, Cantley AM, Yang WS, et al. Ferroptosis: an iron-dependent form of nonapoptotic cell death. *Cell.* 2012;149(5):1060-72.
42. Doll S, Freitas FP, Shah R, Aldrovandi M, da Silva MC, Ingold I, Goya Grocin A, Xavier da Silva TN, Panzilius E, Scheel CH, et al. FSP1 is a glutathione-independent ferroptosis suppressor. *Nature.* 2019;575(7784):693-8.
43. Traverso N, Ricciarelli R, Nitti M, Marengo B, Furfaro AL, Pronzato MA, Marinari UM, and Domenicotti C. Role of glutathione in cancer progression and chemoresistance. *Oxid Med Cell Longev.* 2013;2013(972913.
44. Dringen R. Metabolism and functions of glutathione in brain. *Prog Neurobiol.* 2000;62(6):649-71.
45. Tsuchiya Y, Zhyvoloup A, Bakovic J, Thomas N, Yu BYK, Das S, Orengo C, Newell C, Ward J, Saladino G, et al. Protein CoAlation and antioxidant function of coenzyme A in prokaryotic cells. *Biochem J.* 2018;475(11):1909-37.
46. Tsuchiya Y, Byrne DP, Burgess SG, Bormann J, Bakovic J, Huang Y, Zhyvoloup A, Yu BYK, Peak-Chew S, Tran T, et al. Covalent Aurora A regulation by the metabolic integrator coenzyme A. *Redox Biol.* 2020;28(101318.
47. Yu BYK, Tossounian MA, Hristov SD, Lawrence R, Arora P, Tsuchiya Y, Peak-Chew SY, Filonenko V, Oxenford S, Angell R, et al. Regulation of metastasis suppressor NME1 by a key metabolic cofactor coenzyme A. *Redox Biol.* 2021;44(101978.
48. Bakovic J, Yu BYK, Silva D, Chew SP, Kim S, Ahn SH, Palmer L, Aloum L, Stanzani G, Malanchuk O, et al. A key metabolic integrator, coenzyme A, modulates the activity of peroxiredoxin 5 via covalent modification. *Mol Cell Biochem.* 2019;461(1-2):91-102.
49. Genschel U. Coenzyme A biosynthesis: reconstruction of the pathway in archaea and an evolutionary scenario based on comparative genomics. *Mol Biol Evol.* 2004;21(7):1242-51.
50. Stockwell BR, Friedmann Angeli JP, Bayir H, Bush AI, Conrad M, Dixon SJ, Fulda S, Gascon S, Hatzios SK, Kagan VE, et al. Ferroptosis: A Regulated Cell Death Nexus Linking Metabolism, Redox Biology, and Disease. *Cell.* 2017;171(2):273-85.
51. Viswanathan VS, Ryan MJ, Dhruv HD, Gill S, Eichhoff OM, Seashore-Ludlow B, Kaffenberger SD, Eaton JK, Shimada K, Aguirre AJ, et al. Dependency of a therapy-resistant state of cancer cells on a lipid peroxidase pathway. *Nature.* 2017;547(7664):453-7.

52. Galluzzi L, Vitale I, Aaronson SA, Abrams JM, Adam D, Agostinis P, Alnemri ES, Altucci L, Amelio I, Andrews DW, et al. Molecular mechanisms of cell death: recommendations of the Nomenclature Committee on Cell Death 2018. *Cell Death Differ.* 2018;25(3):486-541.
53. Hayflick SJ, Kurian MA, and Hogarth P. Neurodegeneration with brain iron accumulation. *Handb Clin Neurol.* 2018;147(293-305.
54. Santambrogio P, Ripamonti M, Cozzi A, Raimondi M, Cavestro C, Di Meo I, Rubio A, Taverna S, Tiranti V, and Levi S. Massive iron accumulation in PKAN-derived neurons and astrocytes: light on the human pathological phenotype. *Cell Death Dis.* 2022;13(2):185.
55. Zhang GF, Kombu RS, Kasumov T, Han Y, Sadhukhan S, Zhang J, Sayre LM, Ray D, Gibson KM, Anderson VA, et al. Catabolism of 4-hydroxyacids and 4-hydroxynonenal via 4-hydroxy-4-phosphoacyl-CoAs. *J Biol Chem.* 2009;284(48):33521-34.
56. Li Q, Zhang S, Berthiaume JM, Simons B, and Zhang GF. Novel approach in LC-MS/MS using MRM to generate a full profile of acyl-CoAs: discovery of acyl-dephospho-CoAs. *J Lipid Res.* 2014;55(3):592-602.
57. Prime TA, Forkink M, Logan A, Finichiu PG, McLachlan J, Li Pun PB, Koopman WJ, Larsen L, Latter MJ, Smith RA, et al. A ratiometric fluorescent probe for assessing mitochondrial phospholipid peroxidation within living cells. *Free Radic Biol Med.* 2012;53(3):544-53.

Figure 1 CoA is a specific ferroptosis inhibitor against xCT inhibitors

(**A-B**) CoA supplementation increased the levels of intracellular CoA (**A**) and acetyl-CoA (**B**) as quantified by LC-MS/MS analysis. HT-1080 cells were treated with H2O, CoA (30 μM, 100 μM) for 18 hours for LC-MS/MS analysis. (**C**) CoA inhibited erastin-induced ferroptosis. HT-1080 cells were treated with increasing doses of erastin, either alone or in combination with CoA (100 μM) or deferoxamine (DFO, 80 μM), ferrostatin-1 (Fer-1, 10 μM), liproxstatin-1 (lipro, 2 μM), Trolox (100 μM). The cell viability was quantified by Cell-Titer Glo assay. (**D-E**) Erastin-induced lipid peroxidation (2 µM, 18 hours) in HT-1080 cells was inhibited by CoA treatment as determined by C11-BODIPY staining (**D**) and the quantification of % lipid peroxidation positive cells (**E**). (**F-G**) CoA (100 μM) inhibited erastin (2.5 μM, 20 hours)-induced membrane rupture in HT-1080 cells as observed by CellTox Green under fluorescence microscope (**F**) and quantified by a plate reader (**G**). (**H**) CoA (100 μM) inhibited class 1 FIN (sulfasalazine, SAS, 20 hours)-induced ferroptosis in HT-1080 cells. (**I-J**) CoA (100 μM) inhibited cystine deprivation (24 hours)-induced ferroptosis as determined by Cell-Titer Glo assay (**I**) or CellTox Green assay (**J**). (**K-M**) CoA (100 μM) failed to inhibit ferroptosis in HT-1080 cells induced by RSL3 (class 2 FIN, 20 hours) (**K**), FIN56 (class 3 FIN, 20 hours), and FINO2 (class 4 FIN, 20 hours) (**M**). (**A,B,E,G**) One-way ANOVA, Tukey's multiple comparisons (**C,H,I,J,K,L,M**) Two-way ANOVA, Sidak's multiple comparisons, n = 3 independent biological replicates, *$p < 0.05$, **$p < 0.01$, ***$p < 0.001$, and ****$p < 0.0001$, Data represent mean ± SEM.

Figure 2 CoA regulates mitochondrial thioredoxin system.

(**A**) HT-1080 cells were treated with CoA (100 μM) alone or in combination with the thioredoxin inhibitor ferroptocide (2 μM), during erastin-induced ferroptosis (20 h). Cell viability was quantified using the Cell-Titer Glo assay. (**B**) Thioredoxin reductase activity was significantly reduced following erastin treatment (1.25 μM, 16 h) in HT-1080 cell lysates, and this repression was restored by CoA (100 μM) supplementation. (**C**) Pooled siRNA knockdown of TXN2, but not TXN1, abolished CoA-mediated protection from ferroptosis, indicating a specific role for mitochondrial TXN2. (**D**) Erastin disrupted the interaction between TXNRD2 and TXN2, which was restored by CoA. HT-1080 cells overexpressing TXNRD2 and TXN2 were treated with erastin (2.5 μM, 18 h), with or without CoA, and lysed in NEM buffer for co-immunoprecipitation analysis. (**E**) Western blot analysis revealed that erastin reduced the levels of PRDX3 monomers (reduced, active forms), which was reversed by CoA supplementation. (**F**) Monomer/dimer ratios of PRDX3 were quantified in cells treated with erastin and CoA. (**F**) One-way ANOVA, Tukey's test; (**A–C**) Two-way ANOVA, Sidak's test; n = 3 biological replicates; data are mean ± SEM.

Figure 3 Combined inhibition of glutathione and CoA synthesis leads to synthetic lethality.

(**A**) Knockdown of COASY using two independent siRNAs decreased PRDX3 monomer levels, further linking mitochondrial redox regulation to CoA biosynthesis. (**B**) Quantification of PRDX3 monomer/dimer ratios upon COASY knockdown. (**C**) Stable COASY knockdown sensitized HT-1080 cells to BSO-induced ferroptosis, which was rescued by CoA (100 μM), 4'-phosphopantetheine (4'-PPT, 100 μM), or ferrostatin-1 (10 μM). (**D**) CoA inhibited ferroptosis induced by BSO and PANKi co-treatment. HT-1080 cells were exposed to PANKi (2.5 μM) and increasing doses of BSO with Fer-1, liproxstatin-1 (2 μM), Trolox (100 μM), or CoA (100 μM). (**E–F**) PANKi, but not BSO, increased mitochondrial lipid peroxidation, visualized with mitoPerOx (**E**) and quantified by mean fluorescence intensity (**F**). (**G**) COASY knockdown increased mitochondrial lipid peroxidation, which was rescued by CoA. (**B,F**) One-way ANOVA, Tukey's test; (**C,D,G**) Two-way ANOVA, Sidak's test; n = 3 biological replicates; data are mean ± SEM.

Figure 4 CoA supplement increased CoAlation of TXNRD2 and its interaction with TXN2. (**A**) HT-1080 cells were co-transfected with expression vectors for TXNRD2 (V5-tagged) and TXN2 (Myc-tagged), followed by treatment with Coenzyme A (100 μM) for 18 h. TXNRD2 was immunoprecipitated using anti-V5 beads and analyzed by non-reducing SDS-PAGE. CoAlation was detected with a pan-CoAlation antibody, showing enhanced conjugation upon CoA supplementation. Interaction between TXNRD2 and TXN2 was assessed by probing the V5 pulldown for TXN2 using an anti-Myc antibody. CoA treatment increased TXN2 association, suggesting CoAlation promotes TXNRD2–TXN2 complex formation. (**B**) Confocal microscopy showed that CoA supplement increased TXNRD2-TXN2 interaction in mitochondria. COX IV, mitochondria marker. (**C**) Specificity of CoAlation detection was validated by DTT treatment, which abolished the signal. V5-purified TXNRD2 was incubated with oxidized CoA ± DTT, analyzed by non-reducing PAGE, and immunoblotted. (**D**) CoAlation enhanced thioredoxin reductase activity. Activity was measured using purified TXNRD2 with or without CoAlation or TXNRD inhibitor (auranofin), alongside background (bk) and TrxR(+) control. (**D**) Two-way ANOVA, Sidak's test; $^*p < 0.05$, $^{**}p < 0.01$; n = 3 biological replicates. Bars represent mean ± SEM.

Figure 5 CoAlation of Cys-483 on TXNRD2 protein regulates thioredoxin reductase activity.

(**A**) Tandem mass spectrometry identified the CoA-modified peptide C*GASYAQVMR, localizing the modification to the N-terminal cysteine. (**B**) Relative quantification confirmed increased abundance of the modified peptide in oxidized CoA-treated vs. DMSO samples, confirming C483 CoAlation. (**C**) Mutation of Cys-483 to alanine (C483A) abolished most TXNRD2 CoAlation. Wild-type and mutant proteins were analyzed via non-reducing PAGE and Western blot. (**D**) The C483A mutation also abolished thioredoxin reductase activity, which could not be rescued by oxidized CoA. (**E**) Erastin treatment (2 μM, 16 h) reduced CoAlation levels in HT-1080 cells overexpressing TXNRD2. (**F**) Cys-483 is essential for TXNRD2's anti-ferroptotic function. Cells with TXNRD2 knockout were reconstituted with wild-type or C483A mutant, then treated with erastin (20 h); only wild-type restored viability. (**D,F**) Two-way ANOVA, Sidak's test; $^*p < 0.05$, $^{**}p < 0.01$; n = 3 biological replicates. Bars represent mean ± SEM.

Figure 6 Disruption of CoA biosynthesis in PKAN fibroblasts and OBSC leads to mitochondrial lipid peroxidation.

(**A**) *PANK1* knockdown sensitized HT-1080 cells to BSO treatment. HT-1080 cells with shRNA targeting *PANK1*, *PANK2*, or *PANK3* were treated with BSO for three days for Cell-Titer Glo assay. (**B**) *PANK1*, *PANK2*, and *COASY* knockdown in HT-1080 cells showed an increase in mitochondrial lipid peroxidation. (**C-D**) Primary fibroblasts from PKAN patients and age- and sex-matched unaffected individuals were stained with mitoPerOx, a probe that detects mitochondrial lipid peroxides. Representative images of mitoPerOx staining in (**C**), demonstrating a visibly higher signal intensity in PKAN fibroblasts. Quantification of %

mitoPerOx-positive cells is presented in (**D**), confirming a significant increase in mitochondrial lipid peroxidation in PKAN patient-derived fibroblasts. (**E-F**) The cell death triggered by inhibiting CoA using PANKi in OBSC was rescued by ferrostatin-1. OBSC transfected with YFP were treated with PANKi (2.5 μM) or in combination with ferrostatin-1 (Fer-1, 2 μM, 24 hours). Neuronal viability was assessed by fluorescence microscopy: the number of YFP-positive neurons remaining after treatment was quantified by fluorescence microscopy as a measure of cell survival (**E–F**). Representative images of YFP+ neurons are shown in (**E**), and quantification is presented in **(F**). (**G-H**) The elevated mitochondrial lipid peroxidation by PANKi was rescued by ferrostatin-1. After 1 day of treatment with PANKi (2.5 μM) and Fer-1 (2 μM), OBSC was stained with mitoPerOx (**G**) for quantification (**H**). (**I-J**) PANKi treatment of brain slices repressed the levels of reduced form of PRDX3, which was rescued by Fer-1. OBSC treated with PANKi (2.5 μM) or in combination with Fer-1 (2 μM) were blotted with PRDX3 (**I**) and quantification (**J**). (**B,F,H,J**) One-way ANOVA, Tukey's multiple comparisons (**A**) Two-way ANOVA, Sidak's multiple comparisons, n = 3 independent biological replicates. (**D**)Unpaired t-test. $^{*}p < 0.05$, $^{**}p < 0.01$, $^{***}p < 0.001$, and $^{****}p < 0.0001$, data are mean ± SEM.

Lin_Figure 1

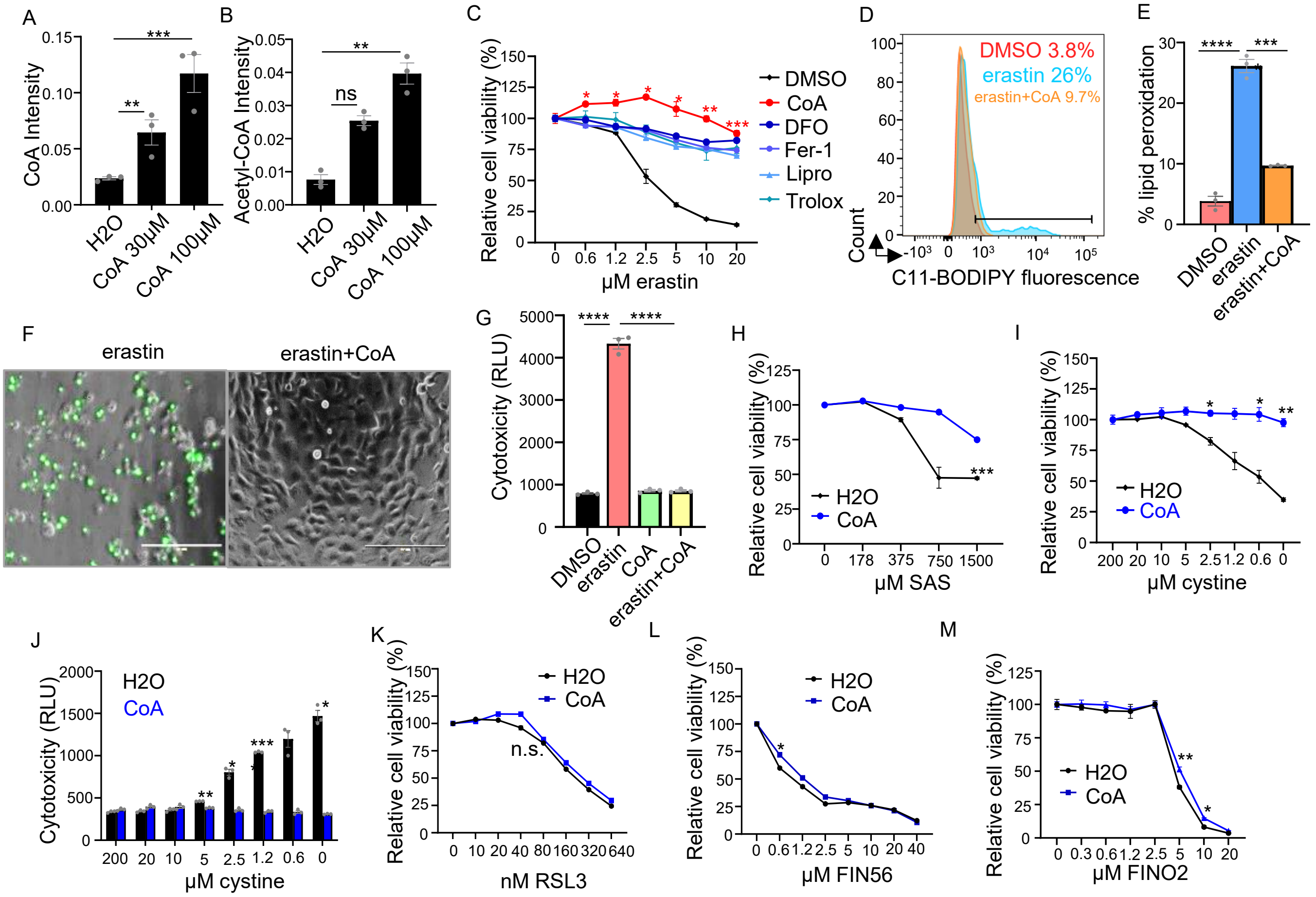

Figure 1 CoA is a specific ferroptosis inhibitor against xCT inhibitors.

(**A-B**) CoA supplementation increased the levels of intracellular CoA (**A**) and acetyl-CoA (**B**) as quantified by LC-MS/MS analysis. HT-1080 cells were treated with H2O, CoA (30 μM, 100 μM) for 18 hours for LC-MS/MS analysis. (**C**) CoA inhibited erastin-induced ferroptosis. HT-1080 cells were treated with increasing doses of erastin, either alone or in combination with CoA (100 μM) or deferoxamine (DFO, 80 μM), ferrostatin-1 (Fer-1, 10 μM), liproxstatin-1 (lipro, 2 μM), Trolox (100 μM). The cell viability was quantified by Cell-Titer Glo assay. (**D-E**) Erastin-induced lipid peroxidation (2 μM, 18 hours) in HT-1080 cells was inhibited by CoA treatment as determined by C11-BODIPY staining (**D**) and the quantification of % lipid peroxidation positive cells (**E**). (**F-G**) CoA (100 μM) inhibited erastin (2.5 μM, 20 hours)-induced membrane rupture in HT-1080 cells as observed by CellTox Green under fluorescence microscope (**F**) and quantified by a plate reader (**G**). (**H**) CoA (100 μM) inhibited class 1 FIN (sulfasalazine, SAS, 20 hours)-induced ferroptosis in HT-1080 cells. (**I-J**) CoA (100 μM) inhibited cystine deprivation (24 hours)-induced ferroptosis as determined by Cell-Titer Glo assay (**I**) or CellTox Green assay (**J**). (**K-M**) CoA (100 μM) failed to inhibit ferroptosis in HT-1080 cells induced by RSL3 (class 2 FIN, 20 hours) (**K**), FIN56 (class 3 FIN, 20 hours), and FINO2 (class 4 FIN, 20 hours) (**M**). (**A,B,E,G**) One-way ANOVA, Tukey's multiple comparisons (**C,H,I,J,K,L,M**) Two-way ANOVA, Sidak's multiple comparisons, $n = 3$ independent biological replicates, *$p < 0.05$, **$p < 0.01$, ***$p < 0.001$, and ****$p < 0.0001$, Data represent mean ± SEM.

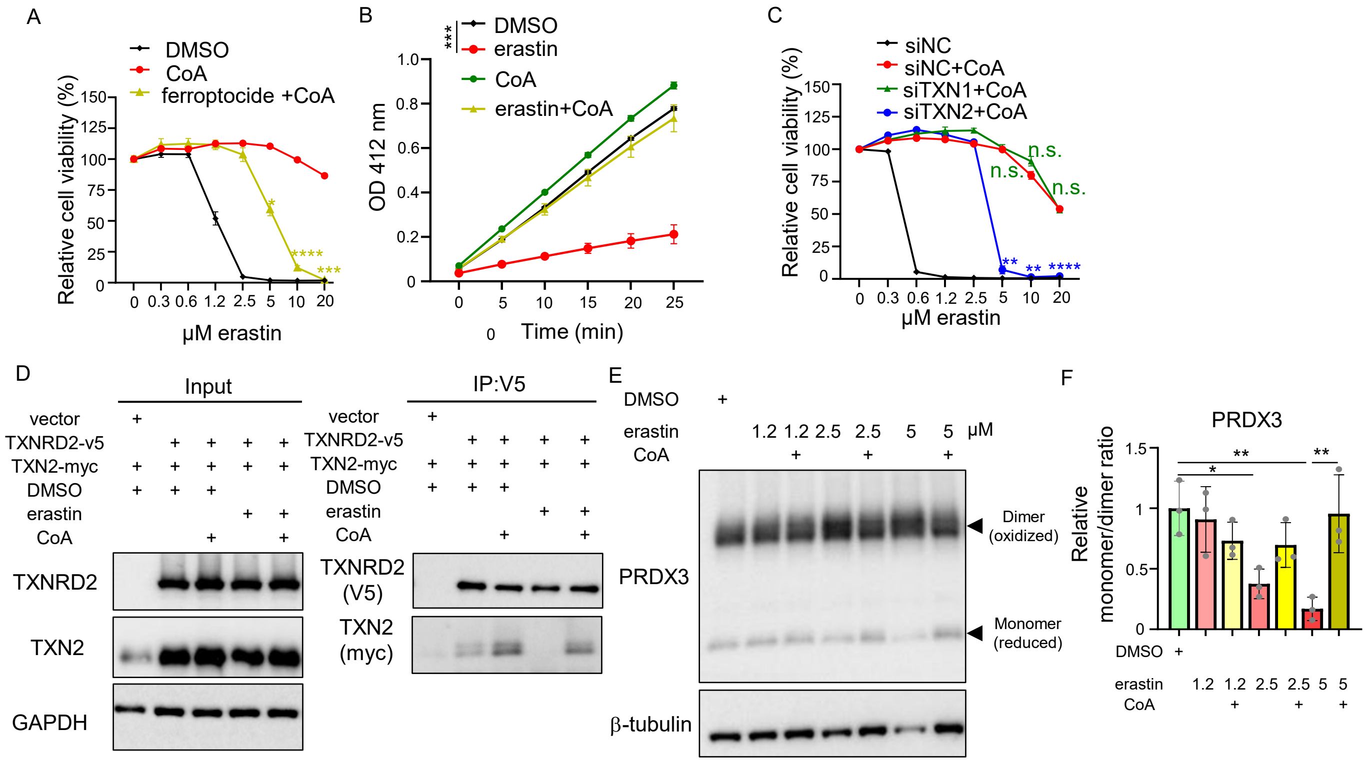

Figure 2 CoA regulates mitochondrial thioredoxin system.

(**A**) HT-1080 cells were treated with CoA (100 μM) alone or in combination with the thioredoxin inhibitor ferroptocide (2 μM), during erastin-induced ferroptosis (20 h). Cell viability was quantified using the Cell-Titer Glo assay. (**B**) Thioredoxin reductase activity was significantly reduced following erastin treatment (1.25 μM, 16 h) in HT-1080 cell lysates, and this repression was restored by CoA (100 μM) supplementation. (**C**) Pooled siRNA knockdown of TXN2, but not TXN1, abolished CoA-mediated protection from ferroptosis, indicating a specific role for mitochondrial TXN2. (**D**) Erastin disrupted the interaction between TXNRD2 and TXN2, which was restored by CoA. HT-1080 cells overexpressing TXNRD2 and TXN2 were treated with erastin (2.5 μM, 18 h), with or without CoA, and lysed in NEM buffer for co-immunoprecipitation analysis. (**E**) Western blot analysis revealed that erastin reduced the levels of PRDX3 monomers (reduced, active forms), which was reversed by CoA supplementation. (**F**) Monomer/dimer ratios of PRDX3 were quantified in cells treated with erastin and CoA. (**F**) One-way ANOVA, Tukey's test; (**A–C**) Two-way ANOVA, Sidak's test; n = 3 biological replicates; data are mean ± SEM.

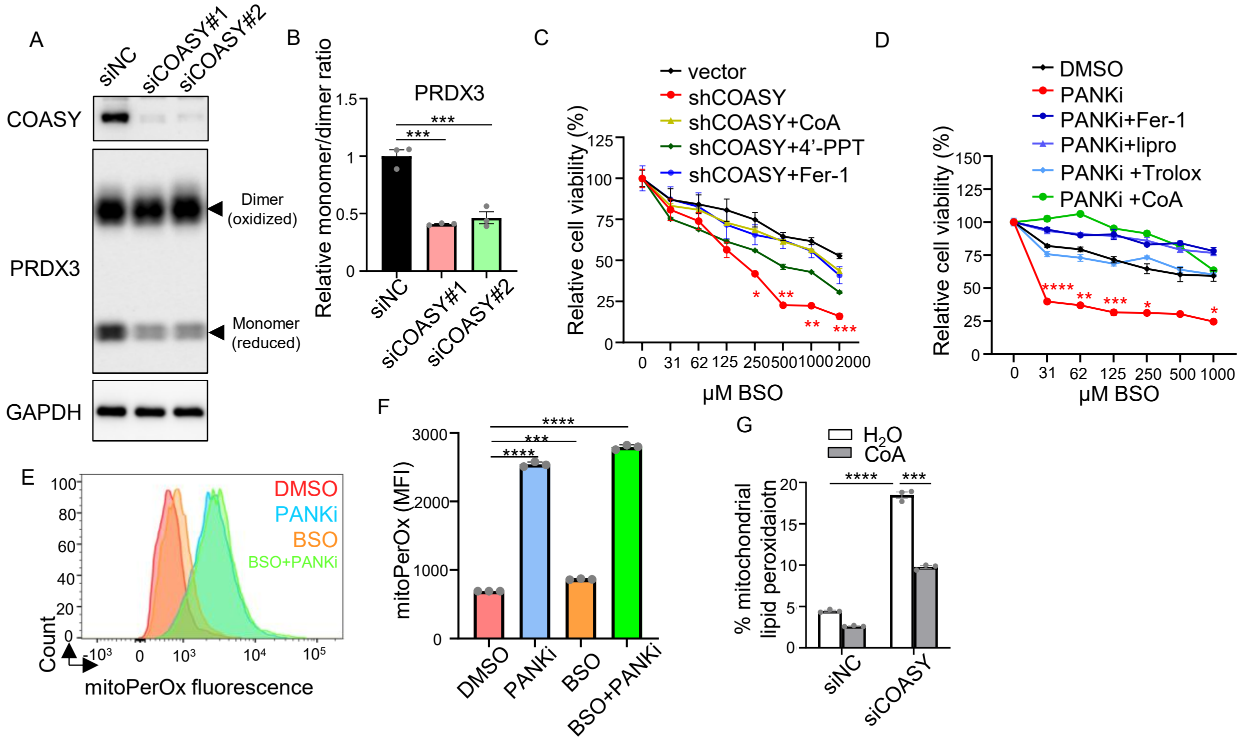

Figure 3 Combined inhibition of glutathione and CoA synthesis leads to synthetic lethality.

(**A**) Knockdown of COASY using two independent siRNAs decreased PRDX3 monomer levels, further linking mitochondrial redox regulation to CoA biosynthesis. (**B**) Quantification of PRDX3 monomer/dimer ratios upon COASY knockdown. (**C**) Stable COASY knockdown sensitized HT-1080 cells to BSO-induced ferroptosis, which was rescued by CoA (100 μM), 4'-phosphopantetheine (4'-PPT, 100 μM), or ferrostatin-1 (10 μM). (**D**) CoA inhibited ferroptosis induced by BSO and PANKi co-treatment. HT-1080 cells were exposed to PANKi (2.5 μM) and increasing doses of BSO with Fer-1, liproxstatin-1 (2 μM), Trolox (100 μM), or CoA (100 μM). (**E–F**) PANKi, but not BSO, increased mitochondrial lipid peroxidation, visualized with mitoPerOx (**E**) and quantified by mean fluorescence intensity (**F**). (**G**) COASY knockdown increased mitochondrial lipid peroxidation, which was rescued by CoA. (**B,F**) One-way ANOVA, Tukey's test; (**C,D,G**) Two-way ANOVA, Sidak's test; n = 3 biological replicates; data are mean ± SEM.

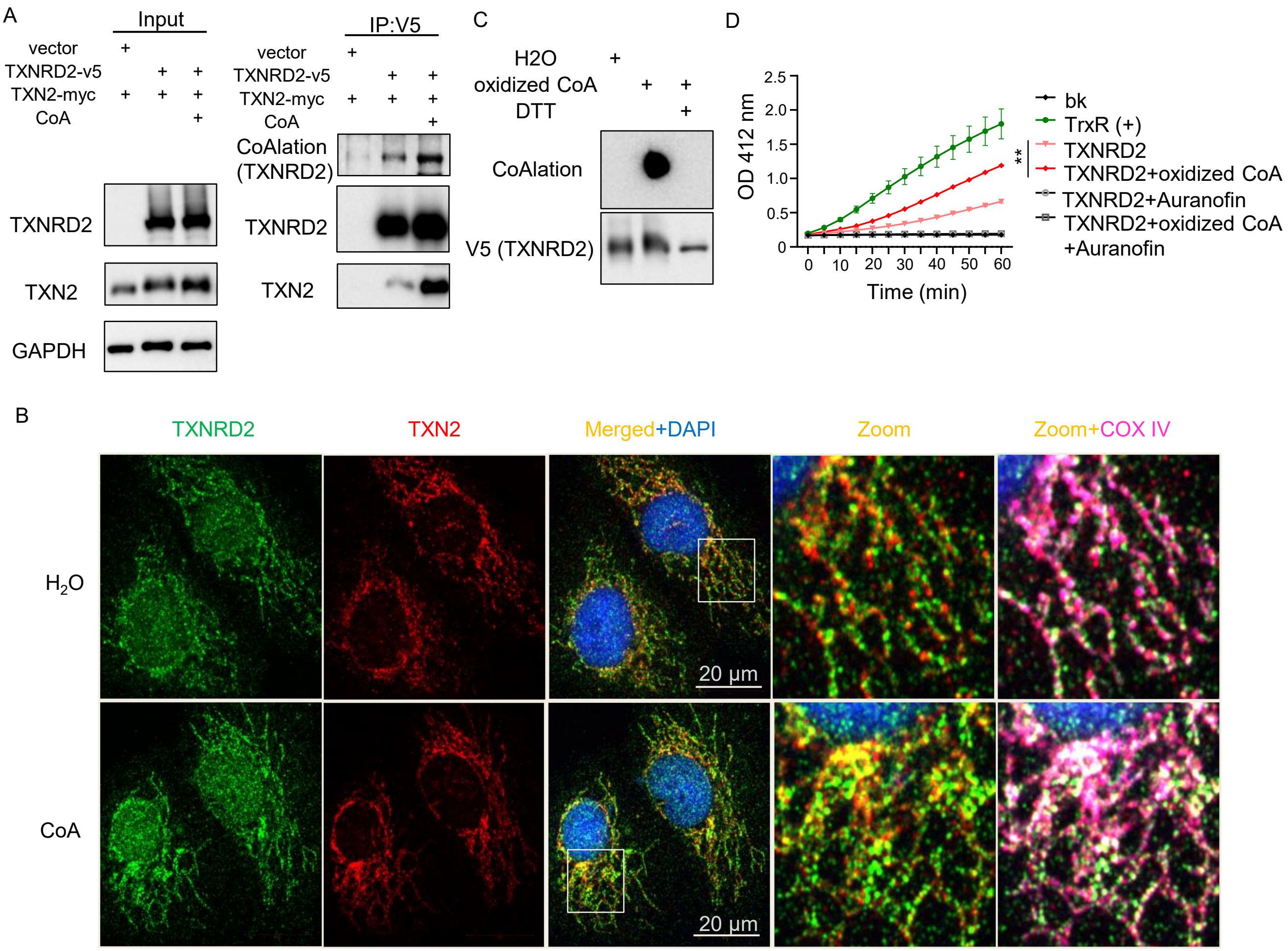

Figure 4 CoA supplement increased CoAlation of TXNRD2 and its interaction with TXN2.
(**A**) HT-1080 cells were co-transfected with expression vectors for TXNRD2 (V5-tagged) and TXN2 (Myc-tagged), followed by treatment with Coenzyme A (100 µM) for 18 h. TXNRD2 was immunoprecipitated using anti-V5 beads and analyzed by non-reducing SDS-PAGE. CoAlation was detected with a pan-CoAlation antibody, showing enhanced conjugation upon CoA supplementation. Interaction between TXNRD2 and TXN2 was assessed by probing the V5 pulldown for TXN2 using an anti-Myc antibody. CoA treatment increased TXN2 association, suggesting CoAlation promotes TXNRD2–TXN2 complex formation. (**B**) Confocal microscopy showed that CoA supplement increased TXNRD2-TXN2 interaction in mitochondria. COX IV, mitochondria marker. (**C**) Specificity of CoAlation detection was validated by DTT treatment, which abolished the signal. V5-purified TXNRD2 was incubated with oxidized CoA ± DTT, analyzed by non-reducing PAGE, and immunoblotted. (**D**) CoAlation enhanced thioredoxin reductase activity. Activity was measured using purified TXNRD2 with or without CoAlation or TXNRD inhibitor (auranofin), alongside background (bk) and TrxR(+) control. (**D**) Two-way ANOVA, Sidak's test; *$p < 0.05$, **$p < 0.01$; $n = 3$ biological replicates. Bars represent mean ± SEM.

Lin_Figure 5

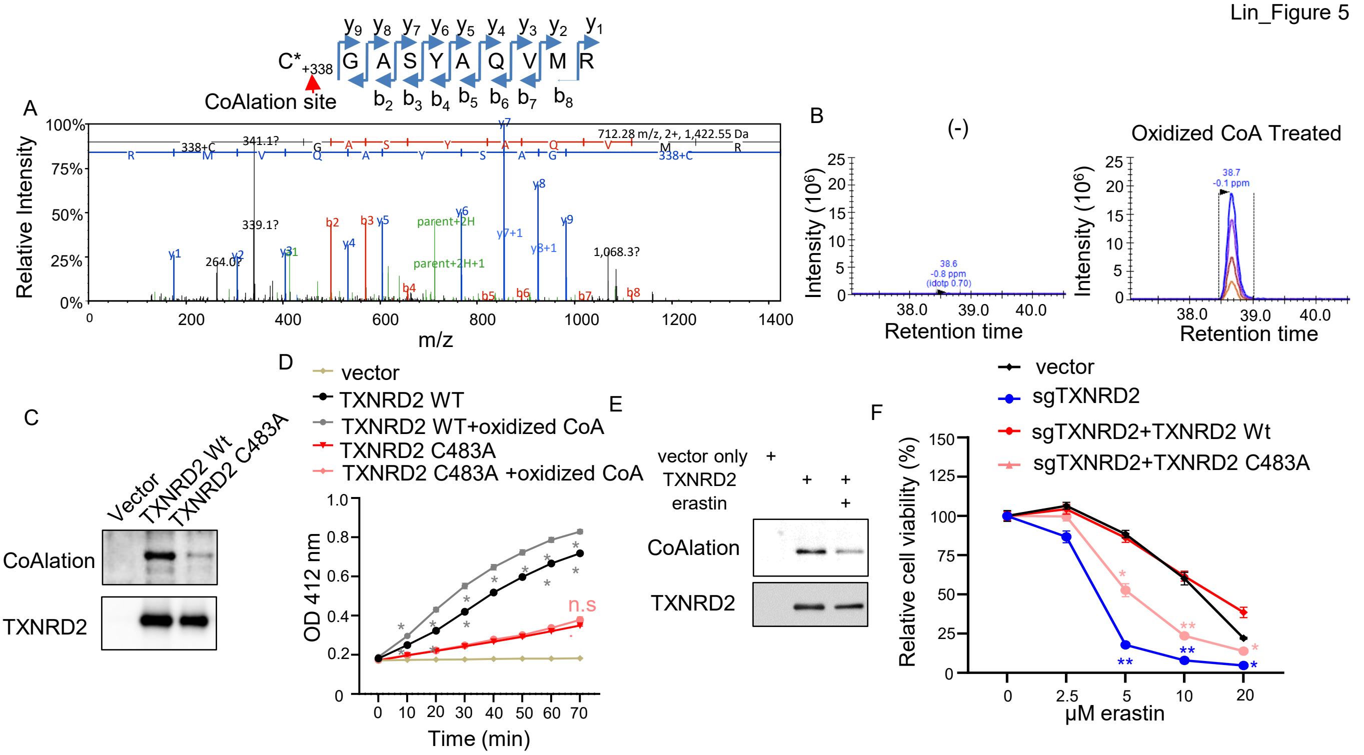

Figure 5 CoAlation of Cys-483 on TXNRD2 protein regulates thioredoxin reductase activity.

(**A**) Tandem mass spectrometry identified the CoA-modified peptide C*GASYAQVMR, localizing the modification to the N-terminal cysteine. (**B**) Relative quantification confirmed increased abundance of the modified peptide in oxidized CoA-treated vs. DMSO samples, confirming C483 CoAlation. (**C**) Mutation of Cys-483 to alanine (C483A) abolished most TXNRD2 CoAlation. Wild-type and mutant proteins were analyzed via non-reducing PAGE and Western blot. (**D**) The C483A mutation also abolished thioredoxin reductase activity, which could not be rescued by oxidized CoA. (**E**) Erastin treatment (2 μM, 16 h) reduced CoAlation levels in HT-1080 cells overexpressing TXNRD2. (**F**) Cys-483 is essential for TXNRD2's anti-ferroptotic function. Cells with TXNRD2 knockout were reconstituted with wild-type or C483A mutant, then treated with erastin (20 h); only wild-type restored viability. (**D,F**) Two-way ANOVA, Sidak's test; $*p < 0.05$, $**p < 0.01$; $n = 3$ biological replicates. Bars represent mean ± SEM.

Lin_Figure 6

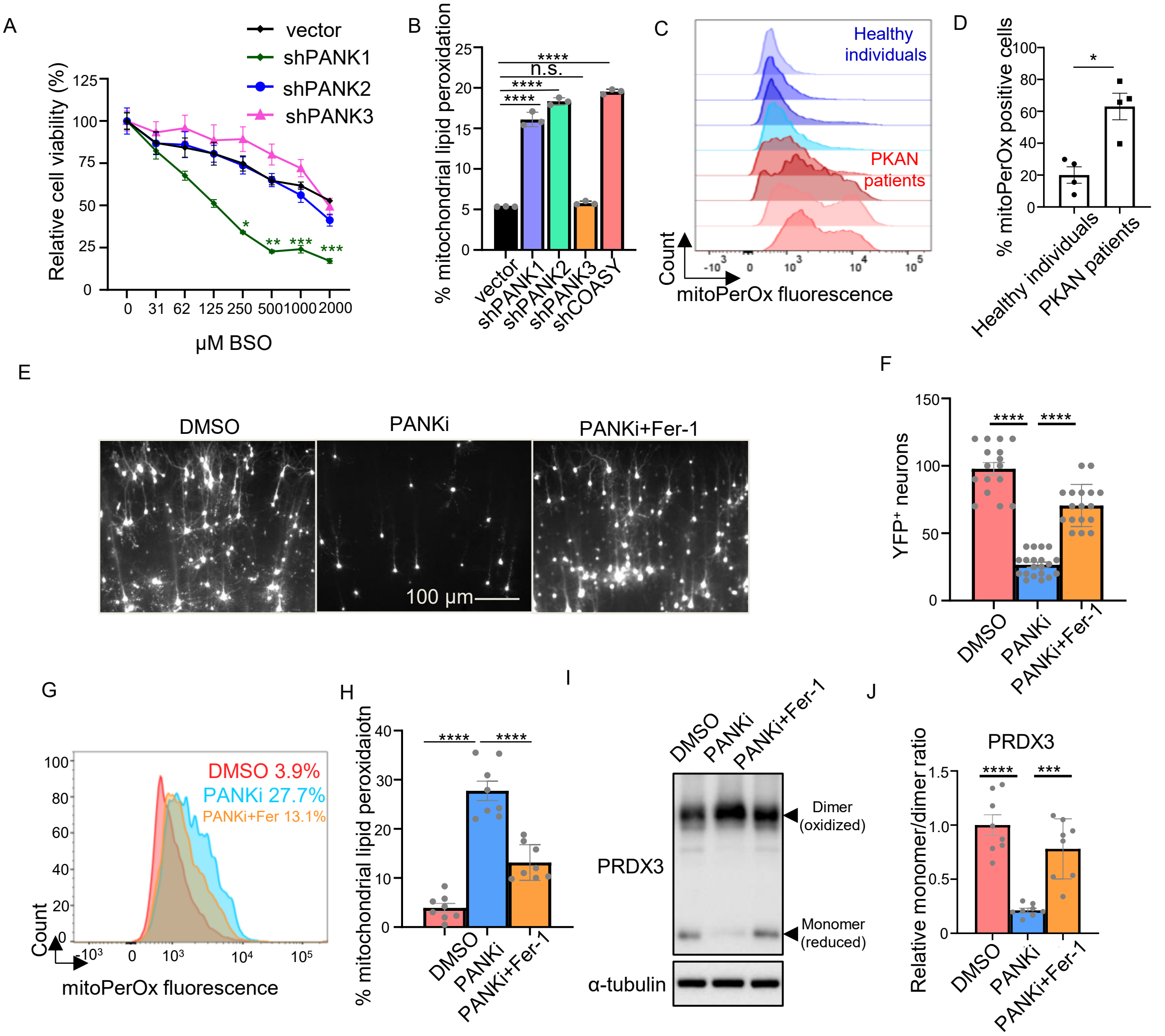

Figure 6 Disruption of CoA biosynthesis in PKAN fibroblasts and OBSC leads to mitochondrial lipid peroxidation.

(**A**) *PANK1* knockdown sensitized HT-1080 cells to BSO treatment. HT-1080 cells with shRNA targeting *PANK1*, *PANK2*, or *PANK3* were treated with BSO for three days for Cell-Titer Glo assay. (**B**) *PANK1*, *PANK2*, and *COASY* knockdown in HT-1080 cells showed an increase in mitochondrial lipid peroxidation. (**C-D**) Primary fibroblasts from PKAN patients and age- and sex-matched unaffected individuals were stained with mitoPerOx, a probe that detects mitochondrial lipid peroxides. Representative images of mitoPerOx staining in (**C**), demonstrating a visibly higher signal intensity in PKAN fibroblasts. Quantification of % mitoPerOx-positive cells is presented in (**D**), confirming a significant increase in mitochondrial lipid peroxidation in PKAN patient-derived fibroblasts. (**E-F**) The cell death triggered by inhibiting CoA using PANKi in OBSC was rescued by ferrostatin-1. OBSC transfected with YFP were treated with PANKi (2.5 μM) or in combination with ferrostatin-1 (Fer-1, 2 μM, 24 hours). Neuronal viability was assessed by fluorescence microscopy: the number of YFP-positive neurons remaining after treatment was quantified by fluorescence microscopy as a measure of cell survival (**E–F**). Representative images of YFP+ neurons are shown in (**E**), and quantification is presented in (**F**). (**G-H**) The elevated mitochondrial lipid peroxidation by PANKi was rescued by ferrostatin-1. After 1 day of treatment with PANKi (2.5 μM) and Fer-1 (2 μM), OBSC was stained with mitoPerOx (**G**) for quantification (**H**). (**I-J**) PANKi treatment of brain slices repressed the levels of reduced form of PRDX3, which was rescued by Fer-1. OBSC treated with PANKi (2.5 μM) or in combination with Fer-1 (2 μM) were blotted with PRDX3 (**I**) and quantification (**J**). (**B,F,H,J**) One-way ANOVA, Tukey's multiple comparisons (**A**) Two-way ANOVA, Sidak's multiple comparisons, n = 3 independent biological replicates. (**D**)Unpaired t-test. $*p < 0.05$, $**p < 0.01$, $***p < 0.001$, and $****p < 0.0001$, data are mean ± SEM.